APPLIED RESEARCH

WILEY

Thermal ablation effects on rotors that characterize functional re-entry cardiac arrhythmia

Eber Dantas[1] | Helcio R. B. Orlande[1] | George S. Dulikravich[2]

[1]Department of Mechanical Engineering, Politécnica/COPPE, Federal University of Rio de Janeiro – UFRJ, Rio de Janeiro, Brazil

[2]Department of Mechanical and Materials Engineering, MAIDROC Lab., Florida International University, Miami, Florida, USA

Correspondence
Helcio R. B. Orlande, Department of Mechanical Engineering, Politécnica/COPPE, Federal University of Rio de Janeiro – UFRJ, Rio de Janeiro, RJ 21941-972, Brazil.
Email: helcio@mecanica.coppe.ufrj.br

Abstract

Thermal ablation is a well-established successful treatment for cardiac arrhythmia, but it still presents limitations that require further studies and developments. In the rotor-driven functional re-entry arrhythmia, tissue heterogeneity results on the generation of spiral/scroll waves and wave break dynamics that may cause dangerous sustainable fibrillation. The selection of the target region to perform thermal ablation to mitigate this type of arrhythmia is challenging, since it considerably affects the local electrophysiology dynamics. This work deals with the numerical simulation of the thermal ablation of a cardiac muscle tissue and its effects on the dynamics of rotor-driven functional re-entry arrhythmia. A non-homogeneous two-dimensional rectangular region is used in the present numerical analysis, where radiofrequency ablation is performed. The electrophysiology problem for the propagation of the action potential in the cardiac tissue is simulated with the Fenton–Karma model. Thermal damage caused to the tissue by the radiofrequency heating is modeled by the Arrhenius equation. The effects of size and position of a heterogeneous region in the original muscle tissue were first analyzed, in order to verify the possible existence of the functional re-entry arrhythmia during the time period considered in the simulations. For each case that exhibited re-entry arrhythmia, six different ablation procedures were analyzed, depending on the position of the radiofrequency electrode and heating time. The obtained results revealed the effects of different model parameters on the existence and possible mitigation of the functional re-entry arrhythmia.

KEYWORDS
cardiac arrhythmia, cardiac muscle electrophysiology, rotor-driven arrhythmia, thermal ablation, thermal damage

1 | INTRODUCTION

Cardiac arrhythmia is the clinical condition of anomalous heartbeat. This generic designation encompasses a vast range of heart diseases that may result in heartbeats mildly slower or faster than normal, as well as abrupt heartbeat variations. Heartbeat variations may either vanish or become severe and uncontrolled, like in the case of fibrillation that may lead to cardiac arrest and death. Arrhythmia can be caused by several abnormalities related to the electrical stimulation of the cardiac tissue, such as[1]: (i) abnormal rhythm generation by the pacemaker cells; (ii) another site in the

heart controlling the contractions (ectopic site) instead of the sinoatrial node; (iii) blockage of the excitation impulse along the conduction pathway; (iv) spontaneous generation of undesired or weakened impulses; or (v) abnormal pathways and patterns of transmission throughout the heart. Ventricular arrhythmia is a major cause of sudden deaths resulting from heart failures, especially in patients with a history of infarction.[2] In 2019, over 315 thousand deaths worldwide were attributed to atrial fibrillation (AF) and flutter, and the global death rate related to those two types of arrhythmia has been steadily increasing since 1990.[3]

Figure 1 shows an illustration of an action potential (AP) for a typical nonpacemaker myocyte. The time between the end of one AP (repolarization) and start of next one (depolarization) is known as diastolic interval (DI). The action potential duration (APD) includes an effective refractory period (ERP), when the cell is not excited by other stimuli. The action potential duration restitution (APDR) denotes the relation between APD and the preceding DI.[4] APDR and the conduction velocity restitution (CVR) have been reported for various tissues of healthy and unhealthy hearts[5,6,7,8,9,10] and are important parameters related to the stimulus propagation in the cardiac tissue.

The *rotor-driven functional re-entry arrhythmia* is one of the various types of arrhythmogenic diseases. It exhibits complicated phenomena of spiral/scroll wave generation and dynamics that can cause dangerous sustainable fibrillation. The rotor-driven functional re-entry arrhythmia is illustrated by Figure 2, where three sequential excitation pulses (S1, S2, and S3) travel from left to right in a medium containing a rectangular region (marked by the yellow rectangle) where the restitution properties are larger than those of the rest of the domain. The stimuli were initiated at times 0 ms (S1), 200 ms (S2), and 320 ms (S3), adjacent to the left wall of the region. Figure 2A–F shows the normalized electric potential at different times, where white and black colors represent the highest and lowest potentials, respectively. After the AP due to the S1 wave ends (i.e., repolarization is completed), a DI is established until the S2 wave excites each cell again (see also Figure 1). The width of the wave caused by S2 in the internal rectangular region in Figure 2A is clearly larger than that of the rest of the domain, because of its larger restitution properties. When the third wave (S3) reaches the internal region, it is still repolarizing from the S2 excitation, while the rest of the domain is normally excited (Figure 2B). Then, wave S3 is disrupted (Figure 2C) generating the spiral shapes observed in Figure 2D that characterize functional re-entry and cause abnormal depolarizations in the opposite direction of the original stimuli (Figure 2E). This process eventually reaches a fibrillatory state with a completely asynchronous excitation pattern (Figure 2F). The AP variations of two points at the central vertical line can be seen in Figure 2G (see Figure 2A–F for the locations of these points, which are marked with the same colors of the AP curves). Similarly to Figure 2A,B, Figure 2G shows that the APD for S2 is longer for the point in the internal region (red curve) than for the point outside this region (green curve). As a result, when S3 reaches the internal point around $t = 500$ ms, it is still in its refractory period and is not affected by the third stimuli. Although Figure 2 presents rotor-driven functional re-entry caused by external stimuli, it is representative of arrhythmia caused by physical activity or heart diseases.

In a review dedicated to the classification of basic mechanisms of cardiac arrhythmia, Antzelevitch and Burashnikov[11] designated the rotor-driven functional re-entry as a disordered movement generated by rotors with no anatomical obstacle (i.e., all tissues are functional). Pandit and Jalife[12] describe how the rotors induce atrial or ventricular fibrillation, while open topics on the subject are discussed by Nattel et al.[13] Rotors are the curved structures created around the wave tip, which can act as a source of fibrillation (asynchronous excitation). Rotors generate vortexes[12] that
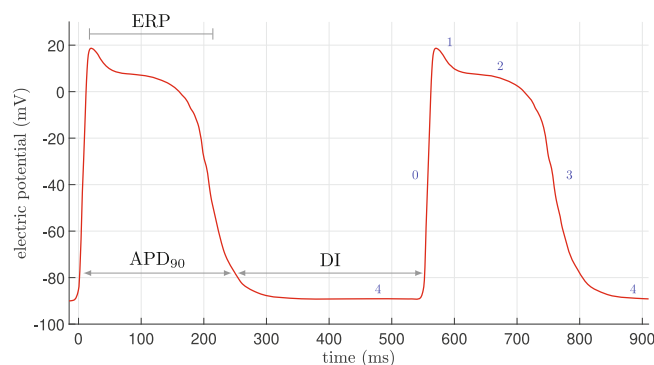
FIGURE 1 Illustration of an action potential (AP) for a typical nonpacemaker myocyte. Numbers refer to the AP phases: resting membrane potential (4), fast depolarization (0), initial repolarization (1), plateau (2), and fast repolarization (3). APD$_{90}$: action potential duration, the subscript means the cut-off was taken at 90% repolarization. DI, diastolic interval; ERP, effective refractory period
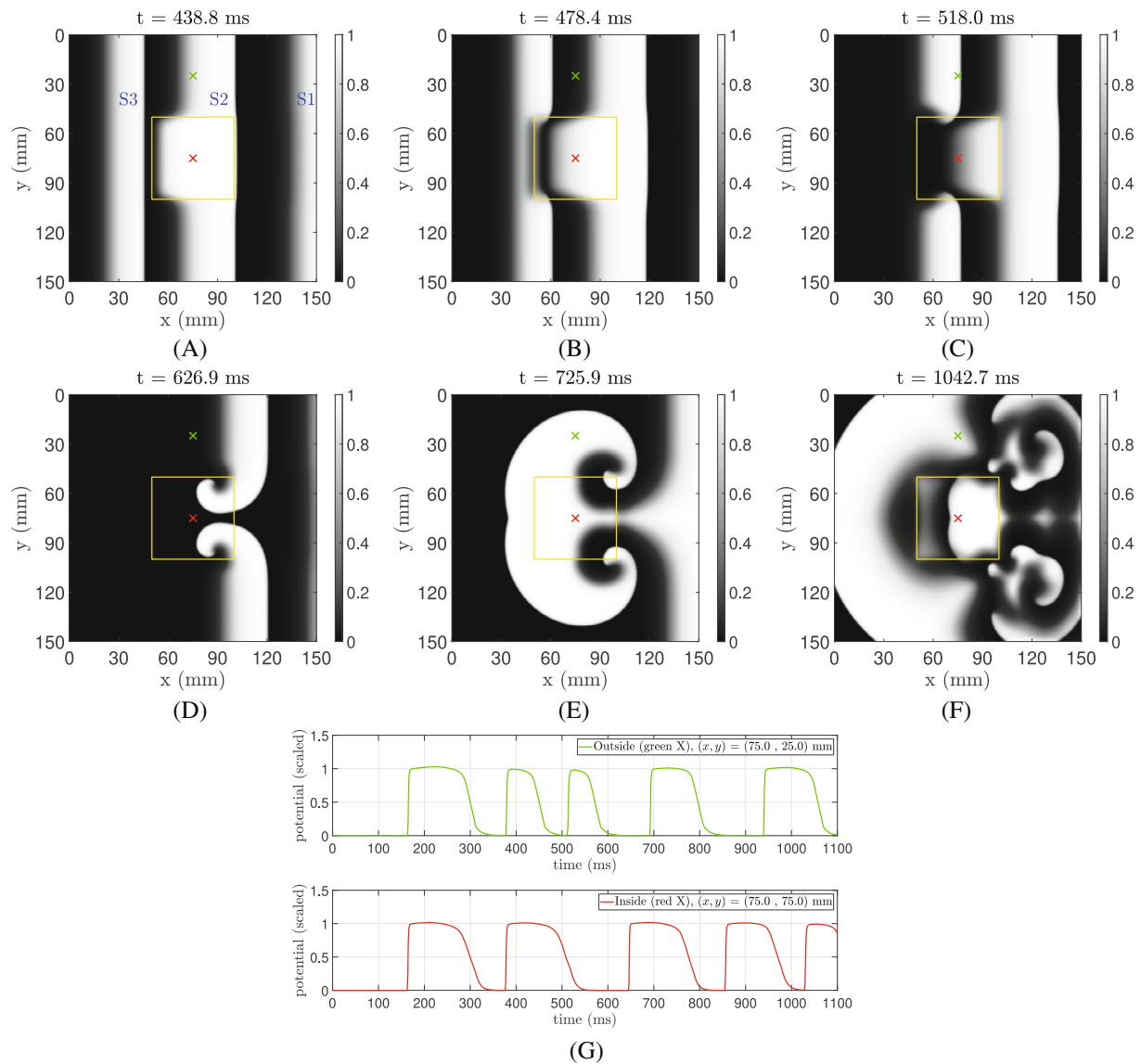
FIGURE 2 Example of rotor-driven functional re-entry arrhythmia. Propagation of the action potential (AP) in a rectangular domain containing an internal region with restitution properties larger than those of the remaining medium. Three stimuli were imposed adjacent to the left border at times 0, 200, and 320 ms. (A–F) Propagation of normalized AP, where white and black colors represent the highest and lowest potentials, respectively. (G) AP variations at two points on the central vertical line: colors indicate the points marked in (A–F)

depend on the curvature of the excitation waves. In two-dimensional problems, the vortexes appear with spiral shapes.[13] In three-dimensional problems, scroll waves are developed and the combination of all spiral tips becomes a one-dimensional curve known as filament (vortex line).[14] The existence of scroll waves and filaments has been demonstrated numerically[15,16] and experimentally.[17]

In the ablation treatment of arrhythmia, electrophysiology properties of a target region in the cardiac muscle are modified by thermal damage to eliminate or minimize undesired electrical conduction, re-entrant cycles or anomalous focal points. Lee et al.[18] described thermal ablation as the main treatment for patients with recurrent symptoms, incessant focal atrial tachycardia, tachycardia-mediated cardiomyopathy, first episode of typical atrial flutter and with flutter after anti-arrhythmic treatment of AF. The success rate of ablation has been reported as $85\% - 90\%$ for atrial tachycardia[18] and idiopathic ventricular tachycardia.[19] However, the efficiency of thermal ablation is highly dependent on the type of arrhythmia. For example, for the case of scar-related ventricular tachycardia there is no optimal strategy to identify the arrhythmogenic substrate,[20] while the success rate of ablation after $3 - 5$ procedures is rather low for patients with persistent AF.[18,21] In their seminal work on the development of personalized virtual-heart technology to guide ablation, Prakosa et al.[22] refer to modest success rates ($50\% - 88\%$) in the elimination of infarct-related ventricular

tachycardia (obstacle re-entry), due to limitations on the precise electrical mapping to identify target regions. Long-term monitoring has also revealed that a significant number of patients continue to suffer asymptomatic AF after ablation,[23] and the success of ablation for AF without medications is $40\% - 60\%$ after 1 year of a single procedure, reaching 70% for 3 or more procedures.[24,25]

Technological advancements must be pursued for optimal localization of target regions in order to improve the success rate of the ablation treatment. In the CONFIRM trials[26,27] accurate targeting of the rotational drivers eliminated or reduced AF by ablation in 86% of 101 cases. In addition, deeper understanding of arrhythmogenic mechanisms are required to improve the success rate of the thermal ablation treatment,[26] particularly for rotor functional re-entry arrhythmia.[13] Spector et al.[28] presented two-dimensional numerical simulations that revealed how spiral re-entry waves could be eliminated when the wavefront reached the border of the domain. In fact, the advancement in computer power enabled the use of numerical simulations of the whole heart for different purposes,[29] including the thermal ablation treatment of arrhythmias.[2,21,22,30,31] However, coupling of different mathematical models of the related multiphysics nonlinear phenomena, as well as numerical simulations under uncertainties,[32] are required to optimally design an individualized thermal ablation treatment for each patient.

The objectives of the present computational work are twofold. First, numerical simulations of the electrophysiology problem are performed to examine the effects of non-homogeneous restitution properties on triggering and sustaining rotor functional re-entry arrhythmia. A two-dimensional rectangular domain is considered here, with an internal rectangular region with larger restitution properties than those of the surrounding medium. A total of 12 cases are simulated with different sizes and positions of the internal region with distinct properties, in order to analyze if rotors are created and how they behave. The second objective of this work is to analyze the effects of the thermal ablation treatment on the elimination of rotor re-entry. For each arrhythmogenic case, six ablation procedures were considered, involving different positions of a radiofrequency electrode and heating times. The electrophysiology problem is modeled in this work with the Fenton–Karma 3V-SIM model.[15] Thermal damage resulting from the radiofrequency heating and heat transfer is considered to follow Arrhenius' model.[33,34]

Novelties of this work include the effects of the thermal damage caused by ablation on the analysis of functional re-entry cardiac arrhythmia. The thermal damage is continuously taken into account in the electrophysiology problem by using the concept of the survival cell ratio,[35] in order to identify a sub-lethal zone that has been experimentally observed.[36,37] Other commonly found approaches are based on a temperature threshold value to distinguish between regions that are thermally damaged or not.[33,36,35] The concept of the survival cell ratio proposed by Pearce[35] is more appropriate than a quite simplistic threshold classification of functional and damaged tissues based on arbitrary values of temperature or thermal damage degree. In fact, threshold values commonly used in the literature for the thermal damage degree are those associated with skin burns by hot water,[38] and cannot be directly related to thermal damage caused to other tissues or by other heating sources.[35]

Due to the importance of the electrophysiology model for this work, a literature review on this topic is briefly presented in the next section and the selection of the Fenton–Karma 3V-SIM model[15] is justified. This section is followed by the definition and formulation of the coupled radiofrequency, heat transfer and electrophysiology problems that are numerically solved with finite control volumes.[39] Results and pertinent discussions for the different cases examined here are then presented and the paper is closed with a section of conclusions that also summarize our contributions.

2 | ELECTROPHYSIOLOGY MODELS

Since the original work of Hodgkin and Huxley[40] electrophysiology models have attracted the attention of different research groups, working with various kinds of excitable cells. Sermesant et al.[41] classified the electrophysiology models as biophysical, phenomenological, and eikonal.

Biophysical models account for the electrical currents through various ion channels across the cell membrane, which are regulated by gate variables, and can consider intracellular structures. The dynamics of the gate variables can be represented by several differential equations that need to be solved for a single cell. Noble[42] adapted the Hodgkin–Huxley formalism to cardiac Purkinje fibers and pacemaker cells. The calcium current that significantly affects the repolarization delay in AP of myocytes (phase 2, see Figure 1), was added in the model of Beeler and Reuter[43] for ventricular fibers. Later, DiFrancesco and Noble[44] vastly expanded the model for 16 dependent variables and more than 30 parameters. Luo and Rudy[45] updated the description of concentration changes and ionic currents to match new experimental results, while also considering the intracellular fluxes related to the sarcoplasmic reticulum. This model has

even been modified to include the effects of genetic diseases.[46] Biophysical models are capable of reproducing complex dynamics observed in cardiac tissue and can reproduce spiral waves.[47]

Phenomenological models are focused on the propagation of excitation waves by treating the spatial domain as continuum, instead of the discrete nature of cells embedded in an extracellular matrix.[48] In bidomain phenomenological models, an intracellular domain is superimposed to an extracellular domain.[49] In the phenomenological monodomain model proposed by Fenton and Karma,[15] the ionic currents are given by:

$$I_{ion} = I_{fi}(U;v) + I_{so}(U) + I_{si}(U;w), \tag{1}$$

where, the fast inward current I_{fi} promotes depolarization and is controlled by the gate variable v. This current represents the fast sodium channels with a gating variable analogous to the ones used in biophysical models. I_{so} is a slow outward current that simulates time-independent potassium currents. The last term in Equation (1) is a slow inward current I_{si} with gate variable w, which represents the calcium transport that occurs mainly in phase 2 of the AP (see Figure 1).

The Fenton–Karma model[15] is capable of representing complicated phenomena with a relatively small number of parameters. In their original[15] and subsequent article,[14] Fenton and Karma refer to their model as 3V-SIM (three variable simplified ionic model). They examined vortex dynamics in two dimensions (spiral waves) and three dimensions (scroll waves). The 3V-SIM model was later modified to a four-variable version by Orovio et al.,[50] which could more accurately reproduce the dynamics of Priebe-Beuckelmann's[51] and Ten-Tusscher's[52] models.

Finally, the simplest electrophysiology model utilizes the eikonal equation,[53] which is given by:

$$F(\mathbf{x})\sqrt{(\nabla t(\mathbf{x}))^T \mathbf{D}(\mathbf{x})\nabla t(\mathbf{x})} = 1, \tag{2}$$

where, $F(\mathbf{x})$ is the local wave speed function, $\mathbf{D}(\mathbf{x})$ is a tensor that models directional anisotropy and the dependent variable is the arrival time $t(\mathbf{x})$ at a position $\mathbf{x}$.

Sermesant et al.[41] have considered multiple wave propagation for the simulation of depolarization followed by repolarization wavefronts. The eikonal model has also been combined with phenomenological models.[54] Chinchapatnam et al.[55] used a different version of Equation (2) termed eikonal-diffusion equation, which included the divergence of the depolarization time. Jacquemet[56] extended the eikonal-diffusion methodology to consider re-entrant arrhythmia, while the refractory and restitution properties of cardiac electrophysiology were implemented in Equation (2) by Pernod et al.[57] These authors modified the multi-front fast marching method for the numerical solution and presented their results for radiofrequency ablation of anatomical re-entry arrhythmias. An approach similar to the eikonal model is to use hybrid cellular automaton with models for the physics of the cardiac tissue stimulation.[28,58]

In a review about numerical techniques for modeling cardiac electrical activity, Plank et al.[48] detailed how the difference of scales between cells and tissues or organs can make the use of biophysical models prohibitive. In addition, biophysical models are complex and the required number of input parameters is large, as opposed to what is preconized in the Principle of Parsimony or Occam's Razor. The classical eikonal model's dependent variable is the time when a point is affected by an imposed stimulus, like the depolarization time by a single wave. Although extensions of the classical eikonal model have been developed as described above, the simplicity and accuracy reported in the literature for the simulation of rotor functional re-entry arrhythmia make phenomenological models as the natural choice to be used in this work.[9,14,15,59,60]

3 | PHYSICAL PROBLEM AND MATHEMATICAL FORMULATION

A two-dimensional rectangular domain was considered for the cases examined in this work, which dealt with: (i) analysis of the electrophysiology behavior and possible generation of rotors due to non-homogeneous restitution properties of functional tissues; and (ii) radiofrequency thermal ablation and heat transfer analyses to quantify local thermal damage and possibly eliminate rotors. Thermal ablation was applied only to those cases where rotors were generated by a rectangular internal region with restitution properties with values larger than those of the surrounding medium.

This section starts with the description and mathematical formulation of the electrophysiology problem. Then, the coupled thermal ablation and heat transfer mathematical formulations are presented, and the thermal damage model is detailed.

3.1 | Electrophysiology problem

In the electrophysiology problem, the transient transmembrane potential $U = U(x,y,t)$ (mV) was computed in a rectangular domain $0 < x < L_x$ and $0 < y < L_y$, which contained an internal rectangular insertion with restitution properties different from those of the base surrounding medium (sizes L_h and H_h in the x and y directions, respectively) as illustrated by Figure 3. The localization of this internal region is given by x_h and y_h. By following the same nomenclature of Nash et al.,[9] the set of electrophysiology properties of the rectangular insertion marked in yellow in Figure 3 was denoted *Steep2*, while the set with the properties of the remaining region was denoted *Steep1*.

The phenomenological 3V-SIM (Fenton–Karma) model[14,15] was used for the electrophysiology problem, which was formulated in terms of the dimensionless transmembrane potential and normalized ionic currents, respectively defined as:

$$u = \frac{U - U_0}{U_{fi} - U_0}, \quad J_a = \frac{I_a}{C_m(U_{fi} - U_0)}, \text{for } a = fi, si, so, \tag{3}$$

where, U_0 is the resting membrane potential (mV), U_{fi} is the Nernst potential (mV, equilibrium) of the fastest inward current, C_m is the membrane capacitance (μF/cm^2), I_a is an ionic current through the membrane (μA/cm^2), and the subscript a denote either one of the three currents considered in the model (Equation (1)).

Boundary conditions were taken as zero fluxes for all surfaces in the electrophysiology problem and the whole domain was assumed initially at null potential. Three stimuli were sequentially imposed at specific times $t_{st,i}$ ($i = 1, 2, 3$) as sources of potential in the region marked in red on Figure 3, during a short time interval δt_{st}, with intensity S (ms^{-1}). The 3V-SIM model as applied to the present physical problem is given by:

$$\frac{\partial u(x,y,t)}{\partial t} = \frac{\partial}{\partial x}\left(D(x,y)\frac{\partial u}{\partial x}\right) + \frac{\partial}{\partial y}\left(D(x,y)\frac{\partial u}{\partial y}\right) - \left(J_{fi}(u,v) + J_{si}(u,w) + J_{so}(u)\right)$$

$$+ S(H(x) - H(x - \delta x_{st}))\sum_{i=1}^{3}(H(t - t_{st,i}) - H(t - t_{st,i} - \delta t_{st})), \text{ for } 0 < x < L_x, \ 0 < y < L_y, \ t > 0; \tag{4a}$$

$$\frac{\partial u}{\partial x} = 0, \quad x = 0 \text{ and } x = L_x, \quad 0 < y < L_y, \quad t > 0; \tag{4b}$$
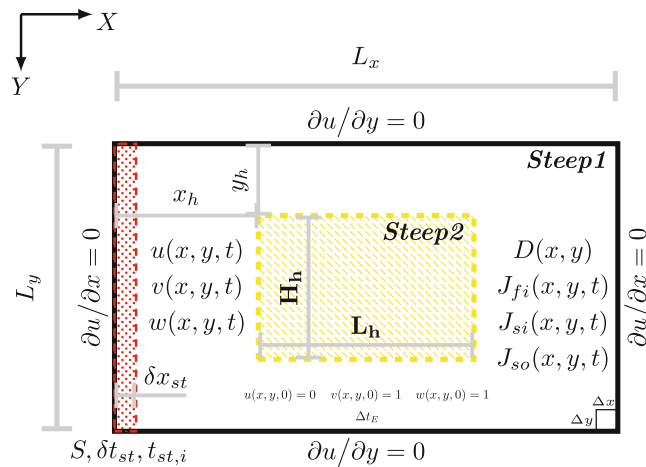

FIGURE 3 Illustration of the electrophysiology problem

$$\frac{\partial u}{\partial y} = 0, \quad 0 < x < L_x \ \ y = 0 \text{ and } y = L_y, \quad t > 0; \tag{4c}$$

$$u = 0, \quad 0 < x < L_x, \quad 0 < y < L_y, \quad t = 0; \tag{4d}$$

$$\frac{\partial v(x,y,t)}{\partial t} = -\frac{v}{\tau_v^+} H(u - u_c) + \frac{1-v}{\tau_v^-(u)} (1 - H(u - u_c)), \ 0 < x < L_x, \ 0 < y < L_y, \ t > 0; \tag{4e}$$

$$\frac{\partial w(x,y,t)}{\partial t} = -\frac{w}{\tau_w^+} H(u - u_c) + \frac{1-w}{\tau_w^-} (1 - H(u - u_c)), \ 0 < x < L_x, \ 0 < y < L_y, \ t > 0; \tag{4f}$$

$$v(x,y,0) = 1 \text{ and } w(x,y,0) = 1, \text{ for } 0 < x < L_x, \ 0 < y < L_y, \ t = 0; \tag{4g}$$

where, the initial conditions for the gate variables v and w were considered uniform and equal to 1, and

$$\tau_v^-(u) = \tau_{v1}^- H(u - u_v) + \tau_{v2}^- (1 - H(u - u_v)). \tag{4h}$$

The current densities were computed with[15,14]:

$$J_{fi}(u,v) = -\frac{v}{\tau_d} (1 - u)(u - u_c) H(u - u_c), \tag{4i}$$

$$J_{si}(u,w) = -\frac{w}{\tau_{si}} \left(\frac{1 + \tanh(c_{si}(u - u_{c,si}))}{2} \right), \tag{4j}$$

$$J_{so}(u) = \frac{1}{\tau_r} H(u - u_c) + \frac{u}{\tau_0} (1 - H(u - u_c)). \tag{4k}$$

In Equation (4a), the transmembrane potential $u(x,y,t)$ for a particular point varies with time due to diffusion and ionic currents that act as source terms. The ionic currents are dependent on $u(x,y,t)$ and also on the gate variables $v(x,y,t)$ and $w(x,y,t)$, which vary according to Equations (4e) and (4f). Three ionic currents are considered in the 3V-SIM model, referred to as fast inward (Equation (4i)), slow inward (Equation (4j)) and slow outward (Equation (4k)). The fast inward current J_{fi} represents the Na$^+$ ion current, responsible for the sudden voltage increase at the onset of the AP (depolarization). The slow inward current J_{si} delays the end of the AP (phase 2) and represents the transport of Ca^{2+} across the cell membrane. Finally, the slow outward current J_{so} reduces the potential during repolarization due to the transport of K$^+$. In Equations (4a)–(4k), $H(z)$ is the Heaviside function ($H(z) = 1$ for $z \geq 0$, $H(z) = 0$ otherwise).

The diffusivity coefficient D (mm^2/ms) in Equation (4a) is actually a combination of three cell properties,[15,61] that is, $D = \sigma_m/(s_v C_m)$, where σ_m is the electrical conductivity of the membrane, s_v is the surface-to-volume ratio and C_m is the membrane capacitance. The diffusion coefficient varies spatially because of the thermal damage promoted by the thermal ablation as it will be apparent below.

3.2 | Thermal ablation

Radiofrequency thermal ablation was applied to all cases that the electrophysiology direct simulations with the 3V-SIM model resulted in re-entry rotors. For the treatment of cardiac arrhythmia, radiofrequency thermal ablation is commonly performed with an electrode that is inserted into the patient in a catheter via the circulatory system. The tip of this electrode is located at the desired position inside the heart, while another dispersive electrode at ground state (0 V) is located over the skin of the patient (in the unipolar case).[37] Heating is more significant around the active electrode where the current density is higher.[37] In addition, for the frequencies commonly employed in radiofrequency ablation the tissues can be considered purely resistive, because the displacement currents are negligible.[33,36,37,62]

For the cases examined in this work, an electrode at constant voltage Φ_e was positioned over the top boundary ($y=0$) and another grounded electrode ($\Phi=0$ V) over the bottom boundary ($y=L_y$), as illustrated by Figure 4. Both electrodes were assumed in perfect contact with the surfaces of the region. The width of the electrode on the top surface was L_e, and its center was located at a distance x_e from the left boundary. The electrode over the bottom boundary had the same width of the region, as an approximation to the electric potential distribution that would result with the grounded electrode located non-intrusively over the patient skin.

A quasi-static formulation was used to model the radiofrequency problem, such that the electric potential $\Phi(x,y,T)$ was obtained as the solution of Laplace's Equation. This solution provides potential values that correspond to the root mean squared value of the radiofrequency voltage.[33] Boundary condition at the bottom surface was imposed as $\Phi=0$ V.[33,62] All the other boundaries were considered with zero current, except where the active electrode was located, which had the voltage imposed as Φ_e ($y=0$ and $x_e - L_e/2 \leq x \leq x_e + L_e/2$). Thus, the radiofrequency problem is given by:

$$\frac{\partial}{\partial x}\left(\sigma(T)\frac{\partial\Phi(x,y,T)}{\partial x}\right) + \frac{\partial}{\partial y}\left(\sigma(T)\frac{\partial\Phi(x,y,T)}{\partial y}\right) = 0, \ 0<x<L_x, \ 0<y<L_y; \tag{5a}$$

$$\frac{\partial\Phi}{\partial x} = 0, \ x=0, \ 0<y<L_y; \tag{5b}$$

$$\frac{\partial\Phi}{\partial x} = 0, \ x=L_x, \ 0<y<L_y; \tag{5c}$$

$$\frac{\partial\Phi}{\partial y} = 0, \ x<x_e - L_e/2 \text{ or } x>x_e + L_e/2, \ y=0; \tag{5d}$$

$$\Phi = \Phi_e, \ x_e - L_e/2 \leq x \leq x_e + L_e/2, \ y=0; \tag{5e}$$

$$\Phi = 0, \ 0<x<L_x, \ y=L_y. \tag{5f}$$

In Equation (5a), $\sigma(T)$ is the electrical conductivity, considered as a function of temperature[62,63,64,65] given by:

$$\sigma(T) = 0.541\exp(0.015(T(x,y,t) - 37)), \ 0 \leq T < 100°C. \tag{6}$$

Therefore, the radiofrequency problem must be solved every time that the temperature distribution in the region is updated, although the problem is steady-state for a given temperature. In fact, the heat transfer and the radiofrequency
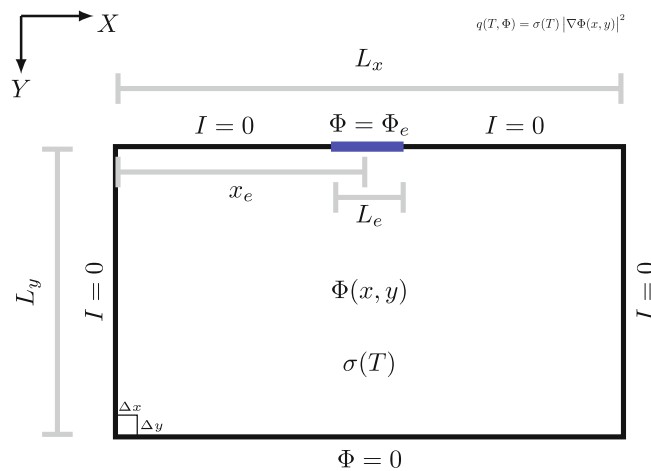

FIGURE 4 Illustration of the radiofrequency problem

problems are coupled not only because of the temperature dependence of the electrical conductivity, but also because of the source term in the region that results from Joule heating, that is,

$$q(T,\Phi) = \sigma(T(x,y,t))|\nabla\Phi(x,y,T)|^2. \tag{7}$$

The classical bioheat transfer model proposed by Pennes[66] has been usually applied for the analysis of cardiac ablation, by discarding metabolic heat generation and blood perfusion.[33,36,67,68,69,70] An enthalpy formulation is required when temperatures in the heated region are raised to 100°C and above.[71,72,73] However, coagulum and char are formed at the electrode-tissue interface when local temperatures exceed 100°C, thus, increasing the electrode impedance and reducing the delivered current. The test-cases examined here were selected so that the temperatures in the region were always below 100°C and, thus, an enthalpy formulation was not required. Although active electrodes are in practice surrounded by the blood flowing inside the heart chamber, they are usually designed with cooling systems to avoid the above heating problems.[74] Gonzalez and Berjano[62] numerically studied models for blood cooling during the thermal ablation. Here, we considered the whole top surface of the domain to be cooled by convection due to the blood flowing inside the heart, including the region where the active electrode was located. The other boundaries were assumed at fixed temperatures, equal to the uniform initial temperature. Figure 5 summarizes the domain and boundary conditions for the thermal problem. The formulation of the heat transfer problem is given next.

$$\rho c \frac{\partial T(x,y,t,\Phi)}{\partial t} = \frac{\partial}{\partial x}\left(k(T)\frac{\partial T}{\partial x}\right) + \frac{\partial}{\partial y}\left(k(T)\frac{\partial T}{\partial y}\right)$$
$$+ q(T,\Phi)(H(t) - H(t - t_h)), \qquad 0 < x < L_x,\ 0 < y < L_y,\ t > 0; \tag{8a}$$

$$T = T_0,\ x = 0,\ 0 < y < L_y,\ t > 0; \tag{8b}$$

$$T = T_0,\ x = L_x,\ 0 < y < L_y,\ t > 0; \tag{8c}$$

$$-k(T)\frac{\partial T}{\partial y} + hT = hT_\infty,\ 0 < x < L_x,\ y = 0,\ t > 0; \tag{8d}$$

$$T = T_0,\ 0 < x < L_x,\ y = L_y,\ t > 0; \tag{8e}$$

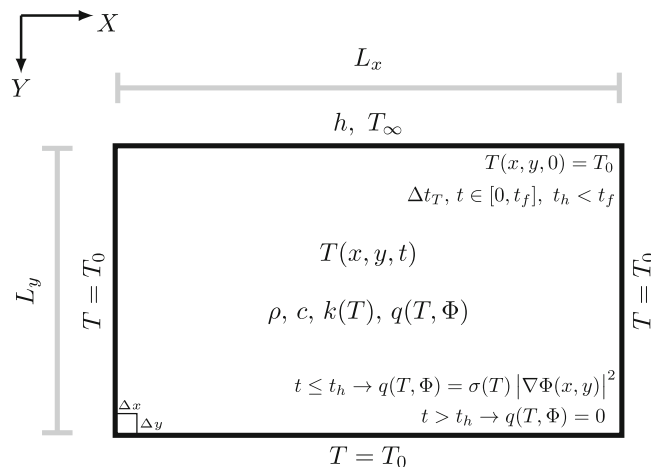$$T = T_0,\ 0 < x < L_x,\ 0 < y < L_y,\ t = 0. \tag{8f}$$

FIGURE 5   Illustration of the thermal problem

where, t_h is the duration of the heating promoted by the radiofrequency problem. In Equations (8a)–(8f), the parameters h, ρ, c and k are the convective heat transfer coefficient (W/(m^{2}K)), tissue density (kg/m^3), specific heat (J/(kgK)) and thermal conductivity (W/(mK)), respectively. The parameters ρ, c and h are considered constant. The thermal conductivity is taken as the following function of temperature[62,64,65,75,76,77]:

$$k(T) = 0.531 + 0.0012(T(x,y,t) - 37), \quad 0 \le T < 100°C. \tag{9}$$

3.3 | Thermal damage

Thermal damage to tissues during cardiac ablation can be classified in three main zones: coagulation necrosis, sub-lethal damage, and original tissue.[36] The coagulation necrosis zone occurs around the electrode and is characterized by severe tissue destruction. The sub-lethal damage zone corresponds to an area of transition to the original tissue, where cells experience apoptosis or recover from reversible damage. Direct damage to the cell membrane is considered as the major cause of necrosis during ablation, together with protein denaturation, inactivation of various enzymes and damage to the mitochondria. Denaturation is considered to occur at temperatures above 40 or 45°C.[36] However, denaturation occurs at different temperatures (and at different rates) for different proteins.[35] As an example, Huang and Miller[37] reported clinical data where reversible tissue damage was observed in a cooled electrode with temperatures of 50 ± 8°C, with permanent damage occurring only at 62 ± 15°C. There are various models to quantify thermal damage and lesion size caused by ablation. The simplest model uses an isotherm that defines the zone of irreversible thermal damage. The most common threshold value used in the literature is 50°C,[33] but it has been recently noticed that such approach overestimates the lesion size in short ablation procedures and underestimates it in long treatments.[33]

The Arrhenius' model is quite popular to represent thermal damage in tissues.[35] It considers not only the temperature levels, but also the time that the tissues are exposed to high temperatures for the prediction of the thermal damage.[33,35] The Arrhenius' model is given by:

$$\Omega(x,y,t) = \int_0^t A \exp\left(-\frac{E_a}{RT(x,y,t')}\right) dt', \tag{10}$$

where, $\Omega(x,y,t)$ is the degree of damage, A is a frequency factor, E_a is the activation energy for the irreversible damage reaction and R is the universal gas constant. Both A and E_a depend on the tissue type, and the thermal damage is highly sensitive to these parameters.[73] The most commonly referenced values for these parameters of cardiac muscle tissue come from an experiment of Jacques and Gaeen[78] during the heating of the ventricular myocardium of a dog.

The Arrhenius model was derived from thermodynamic assumptions frequently used for chemical reactions and it globally accounts for several processes during cell or tissue thermal damage.[34] Although it was originally used to quantify skin burns,[38] it has been successfully applied for various other practical cases.[33,34,35,36] The Arrhenius model was used in this work, but it is noted that other more complicated models can be found in the literature, such as the two-state damage model[79] and stochastic variants.[80]

The values of $\Omega = 0.53$ and 1 were originally associated by Henriques and Moritz[38] with first and second degree skin burns. More recently, Pearce[35] emphasized the broader interpretation of Ω to quantify the fraction of undamaged tissue as:

$$R_\Omega(x,y,t) = \exp(-\Omega(x,y,t)) = \frac{C(t)}{C_0}, \tag{11}$$

where, C_0 is the initial concentration of the original tissue.

In this work, the fraction R_Ω is used to multiply the electrophysiology diffusivity coefficient and the ionic currents of Equations (4a)–(4k) to continuously account for thermal damage effects on the cell capabilities of initiating and transmitting an AP, both in the region of normal cardiac muscle and in the internal rectangular region with distinct electrophysiology properties. This novel approach is different from what is commonly found in the literature, where a threshold value of temperature or Ω is used to binarily set the tissue as either completely undamaged or damaged.[33,35,36]

4 | RESULTS AND DISCUSSIONS

The results obtained in this work are now presented and discussed, first for the effects of size and position of the internal rectangular region, which has electrophysiology properties different from those of the remaining domain, on the generation of rotors as three stimuli are sequentially imposed. Then, six thermal ablation treatments are examined for each case where rotors were generated.

The thickness of the domain was taken as $L_y = 20$ mm, typical of bovine hearts commonly used in experimental studies.[81,62,82] Based on numerical experiments, the length of the domain was fixed as $L_x = 80$ mm, so that the boundary conditions of the thermal problem at $x = 0$ and $x = L_x$ would not affect the temperature field in the region of interest during thermal ablation. With the selected length, the finite domain behaved thermally as an infinite medium along the x direction during the time period of interest. Two heating times were analyzed for the thermal ablation problem: $t_h = 20$ and 30 s, which resulted in maximum temperatures below 75°C. The effects of the radiofrequency ablation on the electrophysiology problem were quantified after 240 s that the heating was started, when the whole region practically became again in thermal equilibrium with its surfaces and the surrounding media at $T_0 = T_\infty = 37$°C (see Equations 8a–8f). Three stimuli were sequentially imposed at times 0 (S1), 200 (S2), and 320 (S3) ms, and the electrophysiology problem was solved up to 1000 ms, when their effects dissipated.

The numerical simulations involved three sizes of the internal rectangular region with electrophysiology properties different from those of the remaining domain, all of them with $H_h = 10$ mm and centered along the x direction (see Figure 6). As for the length of the internal region, it was fixed as $L_h = 10$ mm for cases designated as E1, $L_h = 20$ mm for cases E2 and $L_h = 30$ mm for cases E3. Four distances of the internal region to the top boundary were examined for each of these cases, namely: (A) $y_h = 0$ mm, (B) $y_h = 2$ mm, (C) $y_h = 5$ mm, and (D) $y_h = 8$ mm. Figure 6 sketches all the 12 cases examined in this work, where the yellow rectangle defines the internal region with the distinct electrophysiology properties. Table 1 summarizes several input parameters used for the simulations presented in this work together with the related references. Table 2 presents the electrophysiology properties used for the internal rectangular region (*Steep2*) and for the rest of the domain (*Steep1*), where we followed the same notation used by Nash et al.[9]

The electrophysiology, radiofrequency and thermal problems, given by Equations (4a)–(4k), (5a)–(5f) and (8a)–(8f), respectively, were solved in this work by dedicated finite-volume[39] codes written for MATLAB́ The Alternating-Direction-Implicit (ADI) method[39] was applied for the transient electrophysiology and thermal problems, while the discretized steady-state radiofrequency problem was solved iteratively with the Gauss–Seidel method with SOR.[39] Code verification[83] was performed with analytical solutions for the thermal and radiofrequency problems, considering the whole domain with homogeneous properties. The web applet made available by Fenton et al.[61] was used for code verification of the electrophysiology problem. The region was discretized with finite-volumes of size $\Delta x = \Delta y = 0.1$ mm, while time steps of 1 s and 0.1 ms were used for the thermal and electrophysiology problems, respectively. The maximum Grid Convergence Index (GCI)[83] was 10^{-3} for the temperature at point $x = 39.95$ mm and $y = 0.35$ mm, where temperature gradients were significant during thermal ablation. However, the GCI was in general less than 10^{-4} for the
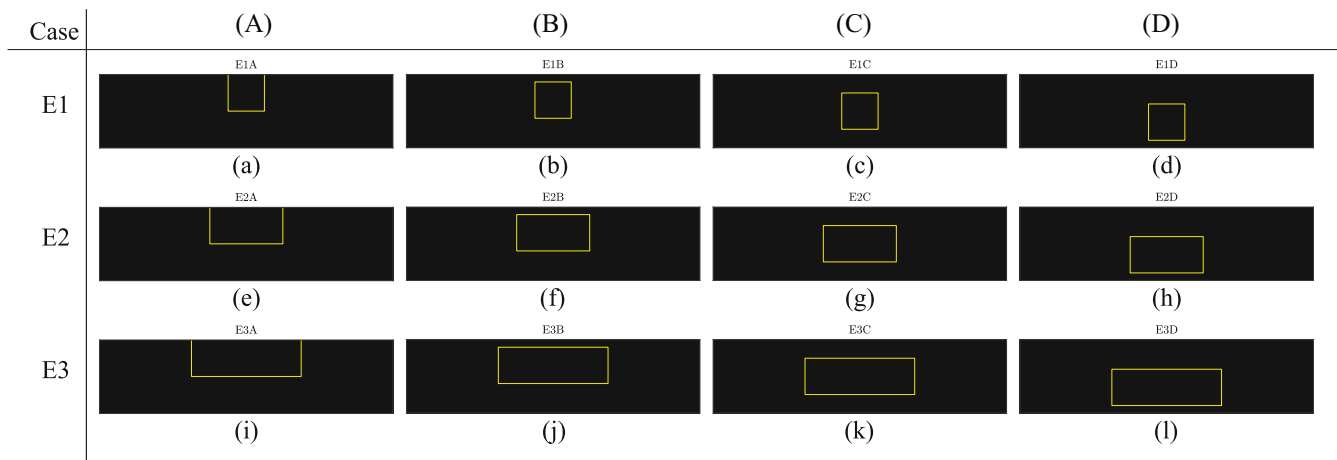
Case	(A)	(B)	(C)	(D)
E1	E1A (a)	E1B (b)	E1C (c)	E1D (d)
E2	E2A (e)	E2B (f)	E2C (g)	E2D (h)
E3	E3A (i)	E3B (j)	E3C (k)	E3D (l)

FIGURE 6 Illustration of all test cases for functional re-entry. Region inside the yellow rectangle with *Steep2* properties and the remaining region with *Steep1* properties

TABLE 1 Input parameters for the simulations

Parameter	Value	Unit	References
ρ	1060	kg/m^3	[62,64,65]
c	3111	J/(kg K)	[62,64,65]
k	Equation (9)	W/(mK)	[62,75,65,64,76,77]
h	610	W/(m^{2}K)	[62]
T_0	37	°C	[33,62]
T_∞	37	°C	[33,62]
t_h	20 or 30	s	–
t_f	240	s	–
x_e	$[25, 55]$	mm	–
Φ_e	25	V	[62]
σ	Equation (6)	S/m	[62–65]
U_0	-85	mV	[9,60,59,15,14]
U_{fi}	15	mV	[9,60,59,15,14]
C_m	1	µF/cm^2	[9,60,59,15,14]
D	0.1	mm^2/ms	[9,60,59,15,14]
δx_{st}	0.5	mm	–
δt_{st}	1	ms	–
$t_{st,i}$	0, 200, 320	ms	[9]
S	0.6	ms^{-1}	–
A	2.94×10^{39}	s^{-1}	[78]
E_a	2.596×10^5	J/mole	[78]

TABLE 2 Electrophysiology properties for the two regions in the domain[15,9,14,60,59]

Parameter	Steep1	Steep2	Unit
τ_d	0.25	0.25	ms
τ_r	33	50	ms
τ_{si}	30	45	ms
τ_0	12.5	8.3	ms
τ_v^+	3.33	3.33	ms
τ_{v1}^-	1250	1000	ms
τ_{v2}^-	19.6	19.2	ms
τ_w^+	870	667	ms
τ_w^-	41	11	ms
u_c	0.13	0.13	–
u_v	0.04	0.055	–
$u_{c,si}$	0.85	0.85	–
c_{si}	10	10	–

temperature at this point at most of the time instants analyzed. The solution of the electrophysiology problem was verified by using APD90 (see Figure 1) at $x = 39.95$ mm and $y = 9.95$ mm in a homogeneous medium with either *Steep1* or *Steep2* properties, resulting in a maximum GCI of 10^{-5}. The joint simulation of the thermal ablation (coupled radiofrequency and thermal problems, $t_h = 30$ s and $t_f = 240$ s), with the subsequent analysis of the thermal damage on the

electrophysiology problem after 1000 ms, required around 7 min of computational time in a computer with CPU Intel Core i5-7600 (3.50 GHz) and 8.0 GB of RAM.

4.1 | Analysis of re-entry rotors

Table 3 presents the results of the electrophysiology simulations for each of the 12 cases shown in Figure 6, regarding the development of re-entry rotors. Table 3 shows that re-entry rotors were not established when the rectangular region with *Steep2* properties was located at the center of the domain (C: $y_h = 5$ mm) for all values considered for L_h (E1, E2, and E3). On the other hand, the opposite behavior was observed when the rectangular region was in contact with the top surface (A: $y_h = 0$ mm) and re-entry was always established. For each L_h, the cases with $y_h = 2$ mm (B) and $y_h = 8$ mm (D) exhibited the same behavior, since they were symmetrically located in the vertical direction and involved distances of 2 mm to the top and bottom surfaces, respectively; for the cases with $L_h = 10$ mm (E1B and E1D) rotors were not established, as opposed to the cases with $L_h = 20$ mm (E2B and E2D) and with $L_h = 30$ mm (E3B and E3D). For the sake of brevity, only representative cases of the behaviors listed above are now discussed.

Figure 7 shows how re-entry rotors sequentially developed for case E1A at different times. It is noticed in Figure 7A that the stimulus S2 induced a long APD in the *Steep2* region. A longer refractory period in this region was induced, which effectively blocked a portion of the excitation wave initiated by S3 and significantly modified the shape of the wavefront, as shown by Figure 7B. Notice in Figure 7B,C that the upper part of the S3 wavefront inside the *Steep2*

TABLE 3 Details of all tested cases for functional re-entry

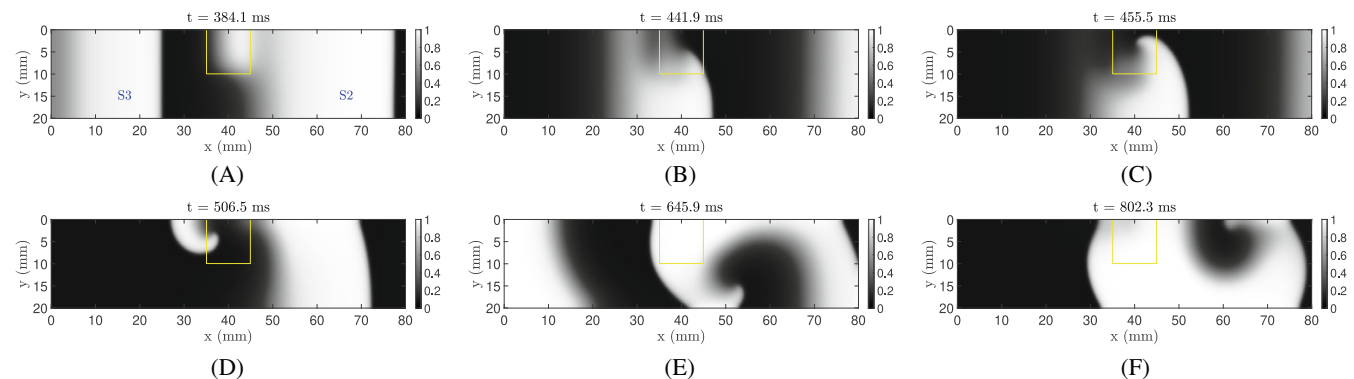| Case		L_h (mm)	x_h (mm)	y_h (mm)	Re-entry?
E1	A	10	35	0	Yes
	B			2	No
	C			5	No
	D			8	No
E2	A	20	30	0	Yes
	B			2	Yes
	C			5	No
	D			8	Yes
E3	A	30	25	0	Yes
	B			2	Yes
	C			5	No
	D			8	Yes

FIGURE 7 Case E1A: $L_h = 10$ mm, $H_h = 10$ mm, $x_h = 35$ mm, $y_h = 0$ mm. Normalized electric potential at different times, where white and black colors represent the highest and lowest potentials, respectively

region completely detached from the top surface, thus, creating the tip of a rotor, which propagated backwards in the domain. The rotor evolved as shown by Figure 7D–F. Similar behaviors were observed with cases E2A ($L_h = 20$ mm) and E3A ($L_h = 30$ mm), but it was noticed that the S3 wavefront tended to detach from the top boundary inside the *Steep2* region sooner (i.e., at smaller x position) as L_h increased.

Rotors were not developed in case E1B, which differed from case E1A by the distance of 2 mm from the *Steep2* region to the top boundary. Figure 8A shows how the wave stimulated by S2 also had a longer APD within the internal region for case E1B, which interfered with the propagation of S3 and modified its intensity and curvature of the wavefront (see also Figure 8B,C). However, such effects did not cause a rotor because the wavefront never detached from the top boundary. Figure 8D–F shows that for case E1B, the S3 wave was able to continue and even rebuild its width, but with a slight change of curvature of the wavefront. On the other hand, rotors were developed for cases E2B and E3B, for which the *Steep2* region was also distant 2 mm from the top boundary, but where $L_h = 20$ mm and $L_h = 30$ mm, respectively. We consider here case E2B. Note in Figure 9A that the effect of the longer APD in the *Steep2* region was more significant for case E2B because the length of this region was twice larger than that for case E1B (see also Figure 8A–D). Thus, the wavefront was broken inside the *Steep2* region (Figure 9B) and rotors were developed and promoted strong backpropagation of the AP (Figure 9C–F).

Rotors were not formed in cases E1C, E2C, and E3C, with the *Steep2* region symmetrically located in the vertical direction ($y_h = 5$ mm). For these cases, the longer APD in the *Steep2* region modified the shape of the subsequent wavefront, but the induced curvatures were not sufficient to detach the wavefront from the top or bottom surfaces and to cause rotors. Such a fact is more evident from the analysis of case E3C, which involved the longest internal region with $L_h = 30$ mm. As for the other cases above, Figure 10A shows the longer APD in the *Steep2* region. The wavefront of S3 was significantly modified inside this region (Figure 10B) but the wave did not break and tended to become more regular as it developed (Figure 10C). Although not presented here, results were also obtained with much longer internal
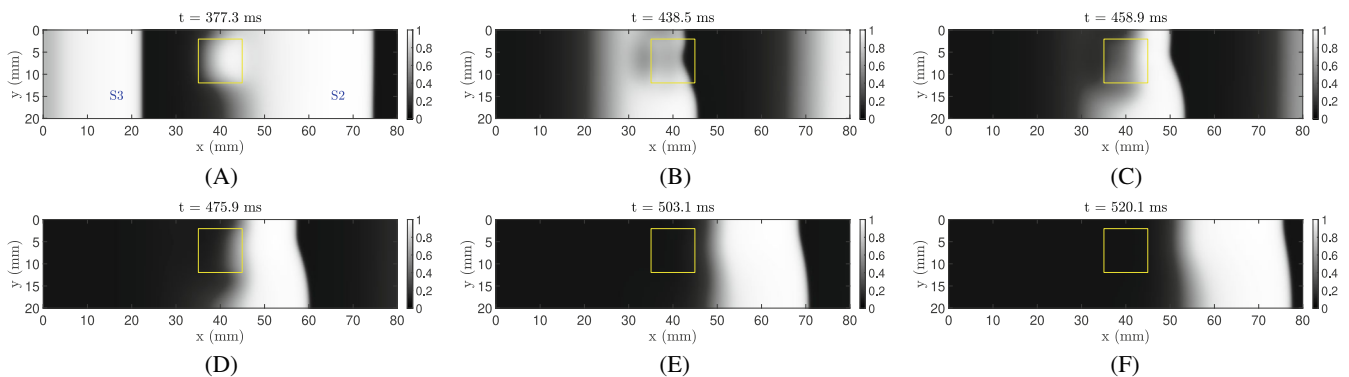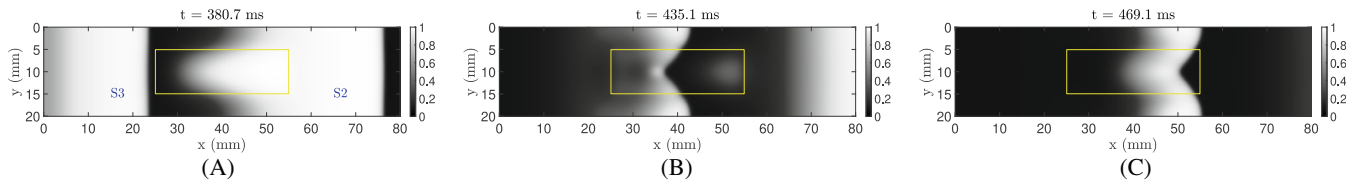

FIGURE 8 Case E1B:. $L_h = 10$ mm, $H_h = 10$ mm, $x_h = 35$ mm, $y_h = 2$ mm. Normalized electric potential at different times, where white and black colors represent the highest and lowest potentials, respectively
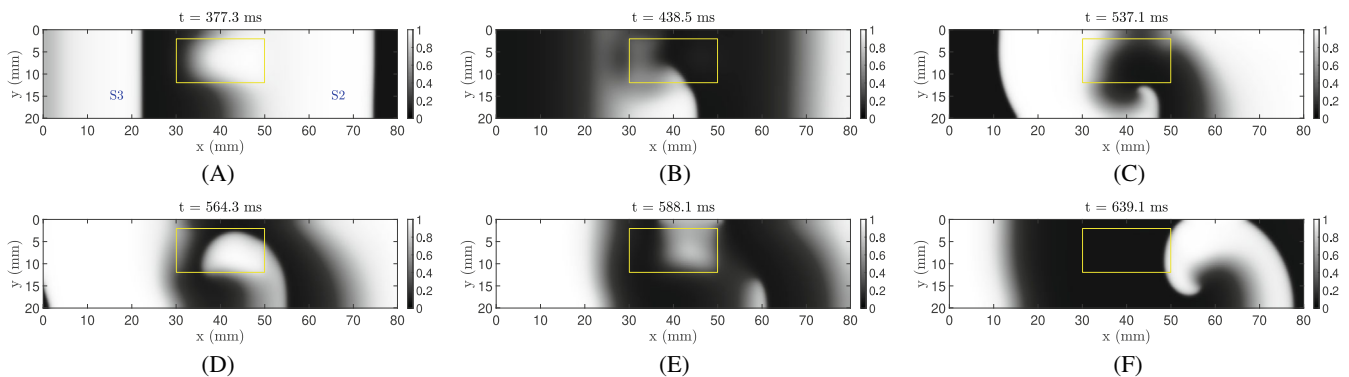

FIGURE 9 Case E2B: $L_h = 20$ mm, $H_h = 10$ mm, $x_h = 30$ mm, $y_h = 2$ mm. Normalized electric potential at different times, where white and black colors represent the highest and lowest potentials, respectively

FIGURE 10 Case E3C, $L_h = 30$ mm, $x_h = 25$ mm, $H_h = 10$ mm, $y_h = 5$ mm. Normalized electric potential at different times, where white and black colors represent the highest and lowest potentials, respectively
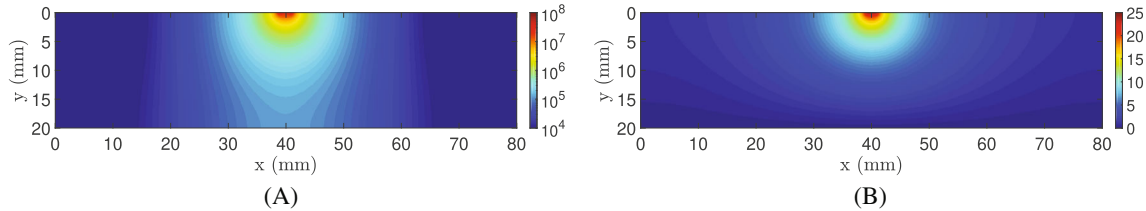
FIGURE 11 Solution of the radiofrequency problem with $T(x,y) = T_0 = 37°C$ and $x_e = 40$ mm: (A) heat source term $q(T, \Phi)$, colors in logarithmic scale with unit W/m^3.; (B) electric potential Φ, colors in linear scale with unit V

regions and $y_h = 5$ mm, but rotors were not formed in any case that the *Steep2* region was symmetrically located in the vertical direction.

The results above revealed that only the internal regions with the *Steep2* properties that had equal distances to the top and bottom boundaries did not generate rotors. Therefore, the symmetry of the internal region in the vertical direction had a fundamental role to avoid the rotor-driven functional arrhythmia. Unfortunately, regions with properties different from those of the remaining cardiac muscle tissue are not likely to be symmetric or to have a regular geometry. Hence, rotors might be generated unless the length of this region is small, such as in cases E1 above where $L_h = 10$ mm.

4.2 | Thermal ablation

Each of the 7 cases detailed in the previous section that exhibited rotor re-entry were subjected to six thermal ablation procedures, numerically simulated with different heating times (t_h) and positions of the active electrode located at the top boundary (x_e, see Figure 4). The heating time was taken as $t_h = 20$ s or $t_h = 30$ s, in order to maintain the maximum temperatures sufficiently below 100°C. As for the electrode position x_e, it was set as aligned with the center or with the vertical edges of the region with the *Steep2* properties.

The thermal damage resulted from the coupled radiofrequency and thermal problems described above. Figure 11A presents the heat source term resulting from the radiofrequency heating with an electrode located at $x_e = 40$ mm, and at the initial time, when the temperature in the region was uniform and equal to 37°C. The largest source term values were symmetrically located around the edges of the electrode, where the voltage gradients were the largest, as given by Equations (5a)–(5f) and demonstrated by Figure 11B. This figure shows the distribution of the electric potential for the uniform temperature of 37°C. Due to the coupling between the radiofrequency and thermal problems caused by the temperature dependence of the electrical conductivity (Equation (6)), the radiofrequency problem was solved every time step when the solution of the thermal problem was obtained, in order to recompute the temperature dependent heat source term. The temperature distribution in the region at the end of the heating period of $t_h = 30$ s and with an electrode located at $x_e = 40$ mm is presented in Figure 12. Figure 12 shows that the largest temperatures were near the electrode, where the radiofrequency source terms were higher (see also Figure 11A). Therefore, the thermal damage was more significant around the electrode and practically null in other regions that were less affected during the heating. Figure 12 also shows that the assigned boundary conditions at $x = 0$, $x = L_x$ and $y = H_y$ did not affect the temperature field during the heating period. The thermal damage in the region will be presented with more details below, in the discussion of the elimination of rotors by ablation.
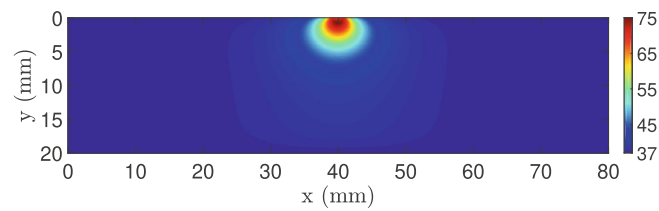
FIGURE 12 Temperature distribution for $t = t_h = 30$ s and $x_e = 40$ mm, colors in linear scale with unit $°C$

TABLE 4 Ablation procedures for case E1A

Case	Ablation procedure	x_e (mm)	t_h (s)	Re-entry after ablation?
E1A	1	35	20	No
	2	35	30	No
	3	40	20	No
	4	40	30	No
	5	45	20	No
	6	45	30	No

Note: Electrode position x_e (mm) and heating time t_h (s). See Figures 3 and 4 for notation.

TABLE 5 Ablation procedures for case E2

Case	Ablation procedure	x_e (mm)	t_h (s)	Re-entry after ablation?
E2A	1	30	20	No
	2	30	30	No
	3	40	20	No
	4	40	30	No
	5	50	20	Yes
	6	50	30	Yes
E2B	1	30	20	No
	2	30	30	No
	3	40	20	No
	4	40	30	No
	5	50	20	Yes
	6	50	30	Yes
E2D	1	30	20	Yes
	2	30	30	Yes
	3	40	20	Yes
	4	40	30	Yes
	5	50	20	Yes
	6	50	30	Yes

Note: Electrode position x_e (mm) and heating time t_h (s). See Figures 3 and 4 for notation.

Tables 4–6 summarize the ablation procedures for the cases with rotors in E1, E2, and E3, respectively. These tables present in their last columns the outcome of the ablation treatments regarding the elimination of rotors. The existence or elimination of rotors was assessed by the numerical simulation of the electrophysiology problem after ablation, during 1000 ms and with three stimuli imposed at times 0 (S1), 200 (S2), and 320 (S3) ms. Table 4 shows that all ablation procedures were successful for E1A ($y_h = 0$ mm), which was the only case with rotors for $L_h = 10$ mm. Notice in Table 5

for E2 ($L_h = 20$ mm) that the ablation procedures successfully eliminated the rotors when the electrode was positioned above the left edge or the center of the region with the *Steep2* properties, except for case E2D. Differently from E2, Table 6 shows that only the ablation with the electrode positioned above the left edge of the *Steep2* region was capable of eliminating the rotors for E3 ($L_h = 30$ mm). None of the ablation procedures examined in this work were able to eliminate the rotors when the vertical position of the *Steep2* region was $y_h = 8$ mm, as presented by Tables 5 and 6, for E2D and E3D, respectively. In fact, the temperature increase was quite small for $y > 7$ mm as illustrated by Figure 12. Therefore, the thermal damage was negligible in the region with the *Steep2* properties for cases E2D and E3D. The red lines appearing in the figures below are contours of $\Omega = 0.2$ (outermost), 1, 2, and 4 (innermost), which represent the fractions of damaged tissue $100(1 - R_\Omega)$ (see Equation (11)) of 18%, 63%, 86%, and 98%, respectively.

Figure 13 presents the evolution of the S2 and S3 waves after the ablation procedure 1 of case E1A. Figure 13B clearly shows how the S3 wave went around the thermally damaged region and then connected back to the top

TABLE 6 Ablation procedures for case E3

Case	Ablation procedure	x_e (mm)	t_h (s)	Re-entry after ablation?
E3A	1	25	20	No
	2	25	30	Yes
	3	40	20	Yes
	4	40	30	Yes
	5	55	20	Yes
	6	55	30	Yes
E3B	1	25	20	No
	2	25	30	No
	3	40	20	Yes
	4	40	30	Yes
	5	55	20	Yes
	6	55	30	Yes
E3D	1	25	20	Yes
	2	25	30	Yes
	3	40	20	Yes
	4	40	30	Yes
	5	55	20	Yes
	6	55	30	Yes

Note: Electrode position x_e (mm) and heating time t_h (s). See Figures 3 and 4 for notation.
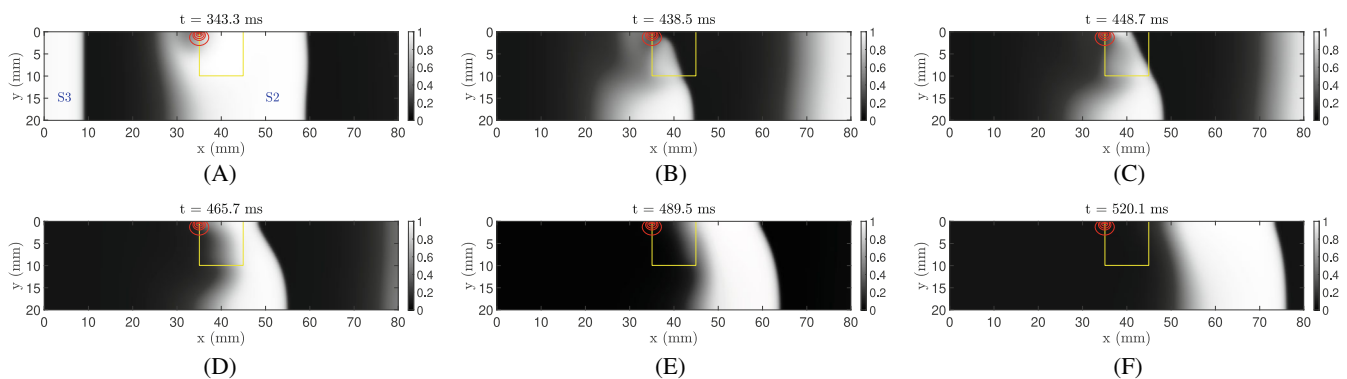
FIGURE 13 Ablation procedure 1 of case E1A: $x_e = 35$ mm, $t_h = 20$ s. Normalized electric potential at different times, where white and black colors represent the highest and lowest potentials, respectively. Red contours represent the fractions of damaged tissue: 18% (outermost), 63%, 86%, and 98% (innermost)

boundary in Figure 13C. The reconnection of the wavefront to the boundary before the rotor tip was formed then reshaped the S3 wave (Figure 13D–F). Although distorted, the S3 wave continued to propagate downstream towards the right boundary and the rotor generation was avoided by the thermally damaged region. Similar behaviors were observed with the other ablation procedures of case E1A. The effects of ablation can also be clearly noticed with the normalized curves of the potential that are presented in Figure 14 for the point $x = 42.05$ mm and $y = 2.05$ mm, which is located inside the region with the *Steep2* properties. For this point, the propagation of the S1 wave had a shorter APD and a longer DI after ablation, although the APs were only slightly modified for S2 and S3. It is interesting to notice in Figure 14 that the small excitation just after S3, which was due to the re-entrant rotor (see Figure 7C), disappeared after the ablation treatment.

The ablation procedure 1 was also successful in the elimination of rotors for cases E2A ($L_h = 20$ mm) and E3A ($L_h = 30$ mm). The results of the ablation procedure 1 for case E2A are presented in Figure 15A–F. Notice in Figure 15A that a weak stimuli induced by the S2 wave split the S3 wave inside the *Steep2* region just after it went around the thermally damaged region (Figure 15B,C). However, the bottom part of the S3 wave reconnected to the top surface before a rotor tip could be formed, and then the S3 wave stably propagated downstream, as shown by Figure 15C–F.

The behavior of the ablation procedure 1 for case E3A was similar to that for case E2A, but a rotor tip tended to be formed in the bottom part of the S3 wave after splitting, because of the longer length of the *Steep2* region, as revealed by Figure 16A–C. The two parts of the S3 wave were reconnected inside the *Steep2* region (Figure 16D) and continued to travel downstream, thus, avoiding the formation of a rotor, as shown by Figure 16E,F. On the other hand, Figure 17A–C shows that the use of a longer heating time (ablation procedure 2) increased the size of the thermally damaged region for case E3A, which completely damped the top part of the S3 wave after it was split. Then, a rotor was formed on the remaining bottom part of the S3 wave when ablation procedure 2 was applied on case E3A (Figure 17D–F).
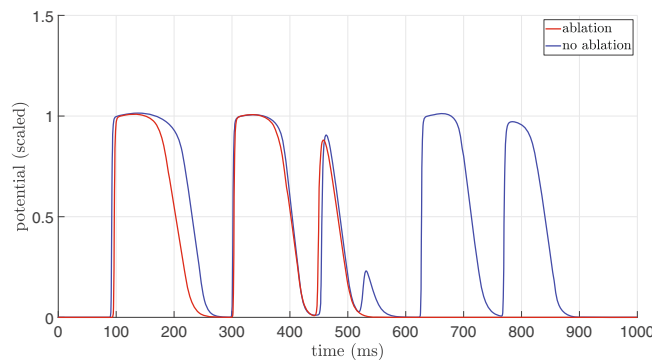

FIGURE 14 Comparison of the potential $u(x = 42.05$ mm, $y = 2.05$ mm, $t)$ before and after ablation 1 for case E1A
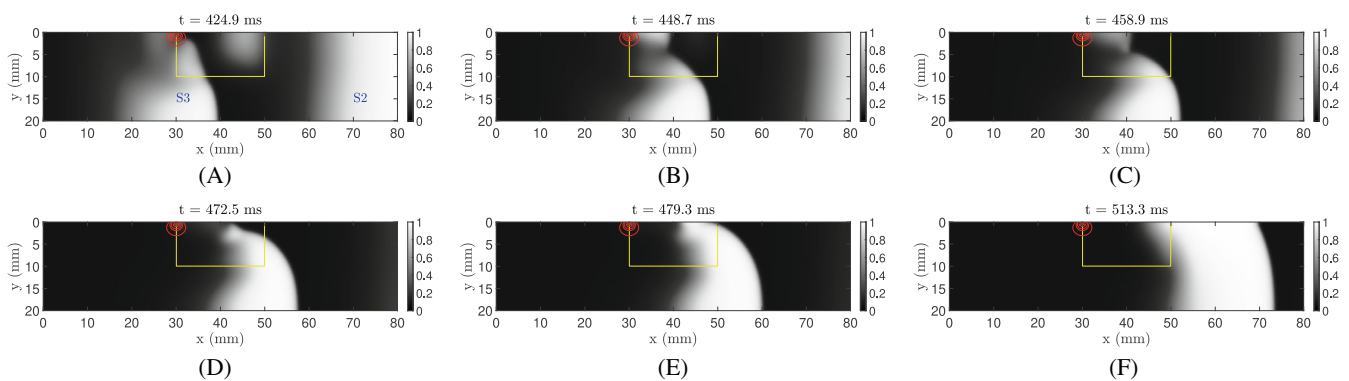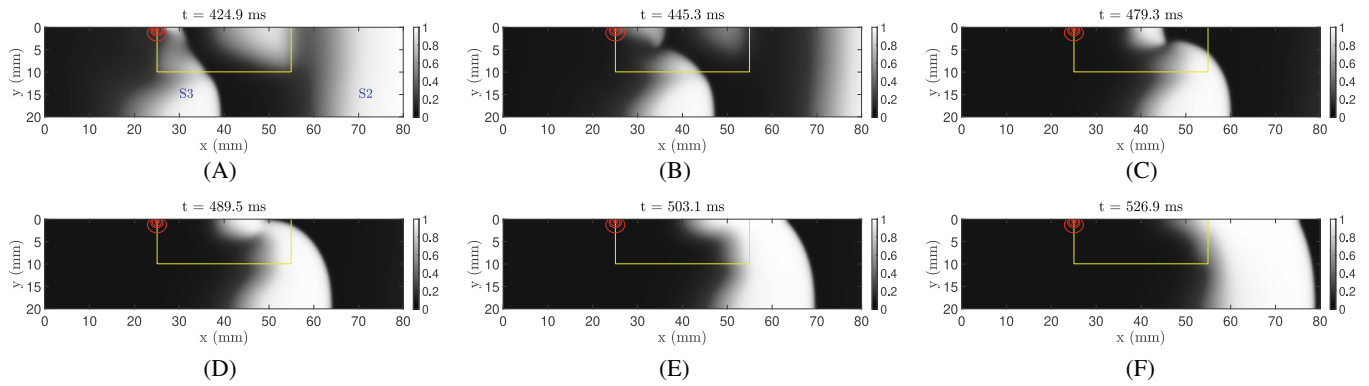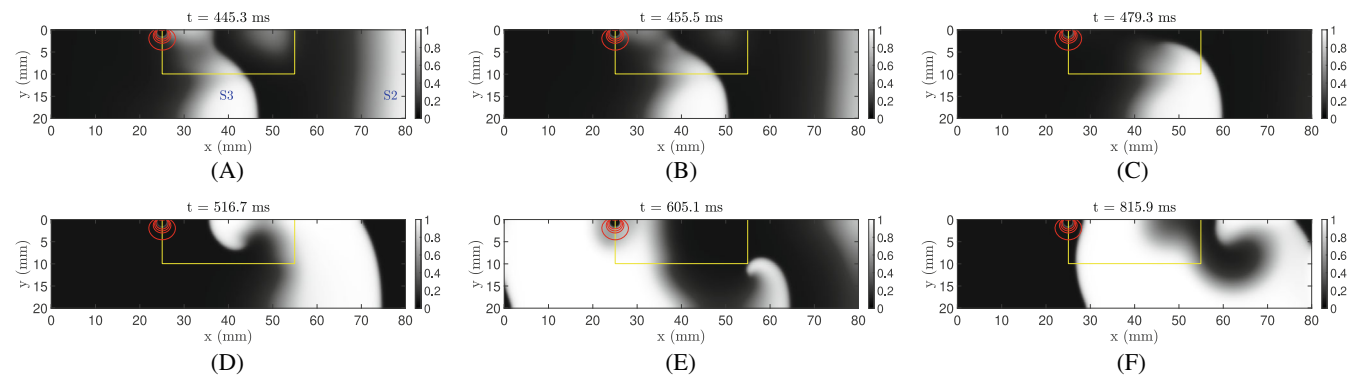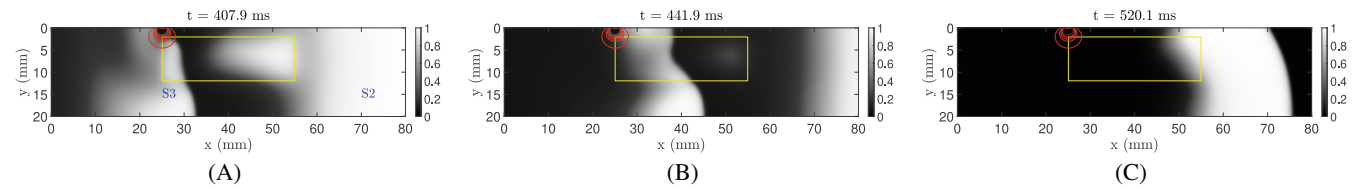

FIGURE 15 Ablation procedure 1 of case E2A: $x_e = 30$ mm, $t_h = 20$ s. Normalized electric potential at different times, where white and black colors represent the highest and lowest potentials, respectively. Red contours represent the fractions of damaged tissue: 18% (outermost), 63%, 86%, and 98% (innermost)
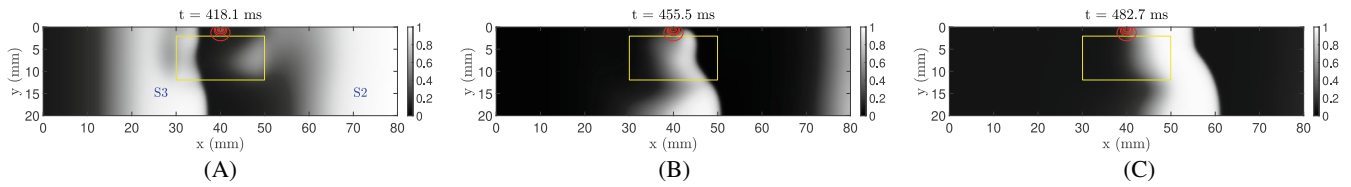
FIGURE 16 Ablation procedure 1 of case E3A: $x_e = 25$ mm, $t_h = 20$ s. Normalized electric potential at different times, where white and black colors represent the highest and lowest potentials, respectively. Red contours represent the fractions of damaged tissue: 18% (outermost), 63%, 86%, and 98% (innermost)
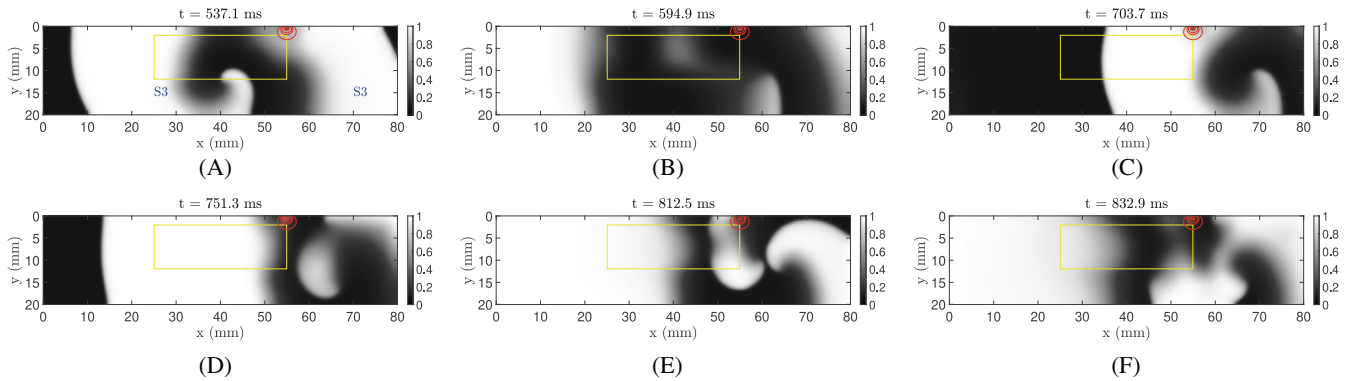

FIGURE 17 Ablation procedure 2 of case E3A: $x_e = 25$ mm, $t_h = 30$ s. Normalized electric potential at different times, where white and black colors represent the highest and lowest potentials, respectively. Red contours represent the fractions of damaged tissue: 18% (outermost), 63%, 86%, and 98% (innermost)

FIGURE 18 Ablation procedure 2 of case E3B: $x_e = 25$ mm, $t_h = 30$ s. Normalized electric potential at different times, where white and black colors represent the highest and lowest potentials, respectively. Red contours represent the fractions of damaged tissue: 18% (outermost), 63%, 86%, and 98% (innermost)

The ablation procedure 1 for cases E2B and E3B behaved similarly as for cases E2A and E3A, respectively. The same took place for ablation procedure 2 for cases E2A and E2B. Thus, these cases are not discussed here for the sake of brevity. On the other hand, the ablation procedure 2 for case E3B avoided the formation of rotors, differently from case E3A (see Figure 17). For case E3B, the largest thermally damaged region obtained with $t_h = 30$ s stabilized the S3 wavefront when the *Steep2* region was 2 mm below the top surface, as presented in Figure 18.

Ablation procedures 3 and 4 with the electrode located at the center of the *Steep2* region were capable of eliminating rotors in case E2B, like procedures 1 and 2. Figure 19A–C presents the ablation procedure 3 for case E2B, where the S3 wave went around the thermally damaged region and reconnected to the top surface. On the other hand, this behavior was distinct with the ablation procedures 3 and 4 for case E3B involving the longest *Steep2* region, because they promoted the thermal damage too downstream of the point where the rotor was formed. For this same reason, ablation

FIGURE 19 Ablation procedure 3 of case E2B: $x_e = 40$ mm, $t_h = 20$ s. Normalized electric potential at different times, where white and black colors represent the highest and lowest potentials, respectively. Red contours represent the fractions of damaged tissue: 18% (outermost), 63%, 86%, and 98% (innermost)

FIGURE 20 Ablation procedure 5 of case E3B: $x_e = 55$ mm, $t_h = 20$ s. Normalized electric potential at different times, where white and black colors represent the highest and lowest potentials, respectively. Red contours represent the fractions of damaged tissue: 18% (outermost), 63%, 86%, and 98% (innermost)

procedures 5 and 6 were not successful in eliminating the rotors in cases E2B and E3B, since the electrode was positioned over the right edge of the *Steep2* region. Ablation procedures 5 and 6 were only successful in case E1A, which had the shortest length ($L_h = 10$ mm). Figure 20 illustrates the complete asynchronous propagation of the original stimuli when ablation procedure 5 was performed in case E3B. In fact, the thermally damaged region promoted further breaks of the wavefront, which can be more clearly seen in Figure 20D, instead of the expected effect of the stabilization of the wavefront.

5 | CONCLUSIONS

This work dealt with numerical analyses of the propagation of electrophysiology stimuli in a rectangular domain, which contained an internal rectangular region with properties different from those of the surrounding cardiac muscle tissue. Such analyses were performed both before and after thermal ablation, which was simulated by coupled radiofrequency and thermal problems. The effects of the thermal ablation on the electrophysiology problem were considered through modifications of the diffusion coefficient and ion currents appearing in the 3V-SIM (Fenton–Karma) phenomenological model used in this work. The thermal damage quantified by an Arrhenius' model was considered to continuously affect such quantities, which had their original values multiplied by the fraction of undamaged tissue, both in the region of normal cardiac muscle and in the internal rectangular region with distinct electrophysiology properties. The electrophysiology, heat transfer and radiofrequency problems were numerically solved by finite-volumes. Code and solution verifications were performed, providing quite small GCI with the selected sizes of finite-volumes and time steps.

The objectives of this work were to verify the generation of re-entry rotors after three sequential stimuli were imposed in the two-dimensional domain, and then examine the possible elimination of rotors by thermal ablation like in the treatment of Functional Re-entry Cardiac Arrhythmia. The generation of rotors was examined for 12 cases, which involved internal regions with different sizes and locations. Then, six different thermal ablation procedures were simulated for each case that exhibited rotors. The ablation procedures involved different heating times and radiofrequency electrode positions, either aligned with the center or with the vertical edges of the internal rectangular

region with distinct electrophysiology properties. The heating times were selected so that the maximum temperatures were below 100°C.

The results presented above revealed that the generation of rotors was highly influenced by the vertical position of the internal region with distinct electrophysiology properties. Regions symmetrically located in the vertical direction (with the same distances to the top and bottom boundaries) did not exhibit rotors. Such was the case even for internal regions with very large lengths. Rotors were generated when the internal region was non-symmetrically located, unless its length was small. On the other hand, rotors were generated for all cases where the internal region was in contact with top boundary of the domain. It was noticed that the rotors were all originated in the third electrophysiology stimulus, when its wavefront detached from the boundaries of the domain, after being significantly disturbed by the longer duration of the AP of the second stimulus.

As for the elimination of rotors by thermal ablation, our results show that all simulated procedures were successful for the smallest internal region considered in this work, which only originally exhibited rotors when it was in contact with the top boundary. The results obtained in this work demonstrated that, from the radiofrequency electrode positions simulated, the best is the one aligned with the upstream (left) edge of the internal region with distinct electrophysiology properties. The simulated ablation treatments with the electrode at this position successfully eliminated the rotors for all cases, except when the longest region was in contact with the top surface and the thermal damage was too large. Such fact revealed that rotors caused by long internal regions are more difficult to eliminate, particularly in this case because the wavefront was broken after it went around the thermal damage. None of the ablation procedures eliminated the rotors when the imposed thermal damage did not reach the internal region with distinct electrophysiology properties, which was too far from the electrode located at the top surface. Perhaps, the use of multiple heating sessions or intrusive electrodes may induce sufficient thermal damage that can eliminate rotors in these cases. We also note that the thermal ablation procedure was not successful if the electrode was located too far downstream from the longitudinal point where the rotor was formed, that is, the rotor was generated and developed without any influence of the thermally damage region. Rotors were eliminated when the incident wave smoothly went around the thermal damage and reattached to the boundary. The treatment was successful even for some cases that the wavefront was mildly disrupted in two parts and then reconnected before moving out of the internal region, which is a possible unstable situation that must be avoided.

Despite the fact that the present work involved a regular two-dimensional geometry, the above conclusions revealed the effects of important parameters regarding the generation and elimination of rotors, like the size and position of the internal region with distinct electrophysiology properties, as well as the position of the radiofrequency electrode. On the other hand, in practice, regions with properties different from those of the remaining cardiac muscle tissue are not likely to be symmetric or to have a regular two-dimensional geometry. Therefore, individual numerical simulations are required for the optimal design of a personalized thermal ablation treatment of the functional re-entry cardiac arrhythmia, based on functional images of the heart. The establishment of a personalized optimal ablation protocol must also include the quantification of simulation uncertainties, such as those of properties used as input parameters for the coupled radiofrequency, heat transfer and electrophysiology models.

CONFLICT OF INTEREST

There are no relationships of all authors with any people or organizations that could inappropriately influence (bias) this work.

DATA AVAILABILITY STATEMENT

The data that support the findings of this study are available from the corresponding author upon reasonable request.

ORCID

Eber Dantas https://orcid.org/0000-0003-2693-0719
Helcio R. B. Orlande https://orcid.org/0000-0002-3511-322X
George S. Dulikravich https://orcid.org/0000-0003-3292-2723

REFERENCES

1. Hall JE. *Guyton and Hall Textbook of Medical Physiology*. 13th ed. Williams & Wilkins; 2016.
2. Arevalo HJ, Vadakkumpadan F, Guallar E, et al. Arrhythmia risk stratification of patients after myocardial infarction using personalized heart models. *Nat Commun*. 2016;7:11437. doi:10.1038/ncomms11437
3. GHDX - Global Health Data Exchange. Death rates associated to atrial fibrillation and flutter, 1990–2019, worldwide and Brazil; 2021. Accessed October, 2021. http://ghdx.healthdata.org/gbd-results-tool?params=gbd-api-2019-permalink/caf7e69f2b49659ea79cc7f678c04a97
4. Weiss JN, Qu Z, Chen PS, et al. The dynamics of cardiac fibrillation. *Circulation*. 2005;112(8):1232-1240. doi:10.1161/CIRCULATIONAHA.104.529545
5. Boyett MR, Jewell BR. A study of the factors responsible for rate-dependent shortening of the action potential in mammalian ventricular muscle. *J Physiol*. 1978;285:359-380. doi:10.1113/jphysiol.1978.sp012576
6. Koller ML, Riccio ML, Gilmour RF Jr. Dynamic restitution of action potential duration during electrical alternans and ventricular fibrillation. *Circulation*. 1998;275(5):H1635-H1642. doi:10.1152/ajpheart.1998.275.5.H1635
7. Kurz RW, Mohabir R, Ren XL, Franz MR. Ischaemia induced alternans of action potential duration in the intact-heart: dependence on coronary flow, preload and cycle length. *Eur Heart J*. 1993;14(10):1410-1420. doi:10.1093/eurheartj/14.10.1410
8. Kurz RW, Ren XL, Franz MR. Dispersion and delay of electrical restitution in the globally ischaemic heart. *Eur Heart J*. 1994;15(4):547-554. doi:10.1093/oxfordjournals.eurheartj.a060541
9. Nash MP, Bradley CP, Sutton PM, et al. Whole heart action potential duration restitution properties in cardiac patients: a combined clinical and modelling study. *Exp Physiol*. 2006;91(2):339-354. doi:10.1113/expphysiol.2005.031070
10. Bárándi L, Virág L, Jost N, et al. Reverse rate-dependent changes are determined by baseline action potential duration in mammalian and human ventricular preparations. *Basic Res Cardiol*. 2010;105:315-323. doi:10.1007/s00395-009-0082-7
11. Antzelevitch C, Burashnikov A. Overview of basic mechanisms of cardiac arrhythmia. *Card Electrophysiol Clin*. 2011;3(1):23-45. doi:10.1016/j.ccep.2010.10.012
12. Pandit SV, Jalife J. Rotors and the dynamics of cardiac fibrillation. *Circ Res*. 2013;112(5):849-862. doi:10.1161/CIRCRESAHA.111.300158
13. Nattel S, Xiong F, Aguilar M. Demystifying rotors and their place in clinical translation of atrial fibrillation mechanisms. *Nat Rev Cardiol*. 2006;14(9):509-520. doi:10.1038/nrcardio.2017.37
14. Fenton FH, Cherry EM, Hastings HM, Evans SJ. Multiple mechanisms of spiral wave breakup in a model of cardiac electrical activity. *Chaos*. 2002;12(3):852-892. doi:10.1063/1.1504242
15. Fenton F, Karma A. Vortex dynamics in three-dimensional continuous myocardium with fiber rotation: filament instability and fibrillation. *Chaos*. 1998;8(1):20-47. doi:10.1063/1.166311
16. Berenfeld O, Pertsov AM. Dynamics of intramural scroll waves in three-dimensional continuous myocardium with rotational anisotropy. *J Theor Biol*. 1999;199(4):383-394. doi:10.1006/jtbi.1999.0965
17. Yamazaki M, Mironov S, Taravant C, et al. Heterogeneous atrial wall thickness and stretch promote scroll waves anchoring during atrial fibrillation. *Cardiovasc Res*. 2012;94(1):48-57. doi:10.1093/cvr/cvr357
18. Lee G, Sanders P, Kalman JM. Catheter ablation of atrial arrhythmias: state of the art. *The Lancet*. 2012;380(9852):P1509-P1519. doi:10.1016/S0140-6736(12)61463-9
19. John RM, Tedrow UB, Koplan BA, et al. Ventricular arrhythmias and sudden cardiac death. *The Lancet*. 2012;380(9852):P1520-P1529. doi:10.1016/S0140-6736(12)61413-5
20. Anter E, Neuzil P, Reddy VY, et al. Ablation of reentry-vulnerable zones determined by left ventricular activation from multiple directions: a novel approach for ventricular tachycardia ablation. *Circ Arrhythm Electrophysiol*. 2020;13(6):23-45. doi:10.1161/CIRCEP.120.008625
21. Boyle PM, Zahid S, Trayanova NA. Towards personalized computational modelling of the fibrotic substrate for atrial arrhythmia. *Europace*. 2016;18(suppl 4):iv136-iv145. doi:10.1093/europace/euw358
22. Prakosa A, Arevalo HJ, Deng D, et al. Personalized virtual-heart technology for guiding the ablation of infarct-related ventricular tachycardia. *Nat Biomed Eng*. 2018;2:732-740. doi:10.1038/s41551-018-0282-2
23. Verma A, Champagne J, Sapp J, et al. Discerning the incidence of symptomatic and asymptomatic episodes of atrial fibrillation before and after catheter ablation (DISCERN AF): a prospective, multicenter study. *JAMA Intern Med*. 2013;173(2):149-156. doi:10.1001/jamainternmed.2013.1561
24. Cheema A, Vasamreddy CR, Dalal D, et al. Long-term single procedure efficacy of catheter ablation of atrial fibrillation. *J Interv Card Electrophysiol*. 2006;15(3):145-155. doi:10.1007/s10840-006-9005-9
25. Weerasooriya R, Khairy P, Litalien J, et al. Catheter ablation for atrial fibrillation. *J Am Coll Cardiol*. 2011;57(2):160-166. doi:10.1016/j.jacc.2010.05.061
26. Narayan SM, Krummen DE, Shivkumar K, Clopton P, Rappel W, Miller JM. Treatment of atrial fibrillation by the ablation of localized sources: CONFIRM (conventional ablation for atrial fibrillation with or without focal impulse and rotor modulation) trial. *J Am Coll Cardiol*. 2012;60(7):628-636. doi:10.1016/j.jacc.2012.05.022
27. Narayan SM, Krummen DE, Rappel W. Clinical mapping approach to diagnose electrical rotors and focal impulse sources for human atrial fibrillation. *J Cardiovasc Electrophysiol*. 2012;23(5):447-454. doi:10.1111/j.1540-8167.2012.02332.x
28. Spector PS, Correa de Sa DD, Tischler ES, et al. Ablation of multi-wavelet re-entry: general principles and in silico analyses. *Europace*. 2012;14(Suppl 5):v106-v111. doi:10.1093/europace/eus278

29. Trayanova NA. Whole-heart modeling: applications to cardiac electrophysiology and electromechanics. *Circ Res*. 2011;108(1):113-128. doi:10.1161/CIRCRESAHA.110.223610

30. Prakosa A, Malamas P, Zhang S, et al. Methodology for image-based reconstruction of ventricular geometry for patient-specific modeling of cardiac electrophysiology. *Prog Biophys Mol Biol*. 2014;115(2–3):226-234. doi:10.1016/j.pbiomolbio.2014.08.009

31. Gurev V, Lee T, Constantino J, Arevalo H, Trayanova NA. Models of cardiac electromechanics based on individual hearts imaging data. *Biomech Model Mechanobiol*. 2011;10(3):295-306. doi:10.1007/s10237-010-0235-5

32. Mirams GR, Pathmanathan P, Gray RA, Challenor P, Clayton RH. Uncertainty and variability in computational and mathematical models of cardiac physiology. *J Physiol*. 2016;594(23):6833-6847. doi:10.1113/JP271671

33. Berjano EJ. Theoretical modeling for radiofrequency ablation: state-of-the-art and challenges for the future. *Biomed Eng Online*. 2006;5:24. doi:10.1186/1475-925X-5-24

34. Pearce JA. Models for thermal damage in tissues: processes and applications. *Crit Rev Biomed Eng*. 2010;38(1):1-20. doi:10.1615/critrevbiomedeng.v38.i1.20

35. Pearce JA. Comparative analysis of mathematical models of cell death and thermal damage processes. *Int J Hyperthermia*. 2013;29(4):262-280. doi:10.3109/02656736.2013.786140

36. Zhang B, Moser MAJ, Zhang EM, Luo Y, Liu C, Zhang W. A review of radiofrequency ablation: large target tissue necrosis and mathematical modelling. *Phys Med*. 2016;32(8):961-971. doi:10.1016/j.ejmp.2016.07.092

37. Huang SKS, Miller JM. *Catheter Ablation of Cardiac Arrhythmias*. 3rd ed. Elsevier; 2014.

38. Henriques FC, Moritz AR. Studies of thermal injury V: the predictability and the significance of thermally induced rate processes leading to irreversible epidermal injury. *Arch Pathol*. 1947;43:489-502.

39. Özişik MN, Orlande HR, Colaço MJ, Cotta RM. *Finite Difference Methods in Heat Transfer*. 2nd ed. CRC Press; 2017.

40. Hodgkin AL, Huxley AF. A quantitative description of membrane current and its application to conduction and excitation in nerve. *J Physiol*. 1952;117(4):500-544. doi:10.1113/jphysiol.1952.sp004764

41. Sermesant M, Konukoglu E, Delingette H, et al. *An Anisotropic Multi-front Fast Marching Method for Real-time Simulation of Cardiac Electrophysiology*. Springer; 2007:160-169.

42. Noble D. A modification of the Hodgkin—Huxley equations applicable to Purkinje fibre action and pacemaker potentials. *J Physiol*. 1962;160(2):317-352. doi:10.1113/jphysiol.1962.sp006849

43. Beeler GW, Reuter H. Reconstruction of the action potential of ventricular myocardial fibres. *J Physiol*. 1977;268(1):177-210. doi:10.1113/jphysiol.1977.sp011853

44. DiFrancesco D, Noble D. A model of cardiac electrical activity incorporating ionic pumps and concentration changes. *Philos Trans R Soc B: Biol Sci*. 1985;307(1133):353-398. doi:10.1098/rstb.1985.0001

45. Luo CH, Rudy Y. A dynamic model of the cardiac ventricular action potential. I. Simulations of ionic currents and concentration changes. *Philos Trans R Soc B: Biol Sci*. 1994;74(6):1071-1096. doi:10.1161/01.RES.74.6.1071

46. Clancy CE, Rudy Y. Linking a genetic defect to its cellular phenotype in a cardiac arrhythmia. *Nature*. 1999;400(6744):566-569. doi:10.1038/23034

47. Courtemanche M, Winfree AT. Re-entrant rotating waves in a Beeler-Reuter based model of two-dimensional cardiac electrical activity. *Int J Bifurcat Chaos*. 1991;1(2):431-444. doi:10.1142/S0218127491000336

48. Plank G, Zhous L, Greenstein JL, et al. From mitochondrial ion channels to arrhythmias in the heart: computational techniques to bridge the spatio-temporal scales. *Philos Trans R Soc A: Math Phys Eng Sci*. 2008;366(1879):3381-3409. doi:10.1098/rsta.2008.0112

49. Courtemanche M. Complex spiral wave dynamics in a spatially distributed ionic model of cardiac electrical activity. *Chaos: Interdiscip J Nonlinear Sci*. 1996;6(4):579-600. doi:10.1063/1.166206

50. Bueno-Orovio A, Cherry EM, Fenton FH. Minimal model for human ventricular action potentials in tissue. *J Theor Biol*. 2008;253(3):544-560. doi:10.1016/j.jtbi.2008.03.029

51. Priebe L, Beuckelmann DJ. Simulation study of cellular electric properties in heart failure. *Circ Res*. 1998;82(11):1206-1223. doi:10.1161/01.RES.82.11.1206

52. Tusschert KHWJ, Noble D, Noble PJ, Panfilov AV. A model for human ventricular tissue. *Am J Physiol-Heart Circ Phys Ther*. 2004;286(4):H1573-H1589. doi:10.1152/ajpheart.00794.2003

53. Keener J, Sneyd J. *Mathematical Physiology*. 2nd ed. Springer; 2009.

54. Franzone PC, Guerri L, Rovida S. Wavefront propagation in an activation model of the anisotropic cardiac tissue: asymptotic analysis and numerical simulations. *J Math Biol*. 1990;28(2):121-176. doi:10.1007/BF00163143

55. Chinchapatnam P, Rhode KS, Ginks M, et al. Model-based imaging of cardiac apparent conductivity and local conduction velocity for diagnosis and planning of therapy. *IEEE Trans Med Imaging*. 2008;27(11):1631-1642. doi:10.1109/TMI.2008.2004644

56. Jacquemet V. An eikonal approach for the initiation of reentrant cardiac propagation in reaction-diffusion models. *IEEE Trans Biomed Eng*. 2010;57(9):2090-2098. doi:10.1109/TBME.2010.2051156

57. Pernod E, Sermesant M, Konukoglu E, Relan J, Delingette H, Ayache N. A multi-front eikonal model of cardiac electrophysiology for interactive simulation of radio-frequency ablation. *Comput Graph*. 2011;35(2):431-440. doi:10.1016/j.cag.2011.01.008

58. Spector PS, Habel N, Sobel BE, Bates JHT. Emergence of complex behavior: an interactive model of cardiac excitation provides a powerful tool for understanding electric propagation. *Circ Arrhythm Electrophysiol*. 2011;4(4):586-591. doi:10.1161/circep.110.961524

59. Clayton RH, Taggart P. Regional differences in APD restitution can initiate wavebreak and re-entry in cardiac tissue: a computational study. *Biomed Eng Online*. 2005;4(1):54. doi:10.1186/1475-925X-4-54

60. Clayton RH, Holden AV. A method to quantify the dynamics and complexity of re-entry in computational models of ventricular fibrillation. *Phys Med Biol*. 2002;47(2):225-238. doi:10.1088/0031-9155/47/2/304

61. Fenton FH, Cherry EM, Hastings HM, Evans SJ. Real-time computer simulations of excitable media: JAVA as a scientific language and as a wrapper for C and FORTRAN programs. *BioSystems*. 2002;64(1–3):73-96. doi:10.1016/s0303-2647(01)00177-0

62. González-Suárez A, Berjano E. Comparative analysis of different methods of modeling the thermal effect of circulating blood flow during RF cardiac ablation. *IEEE Trans Biomed Eng*. 2016;63(2):250-259. doi:10.1109/TBME.2015.2451178

63. Trujillo M, Berjano E. Review of the mathematical functions used to model the temperature dependence of electrical and thermal conductivities of biological tissue in radiofrequency ablation. *Int J Hyperthermia*. 2013;29(6):590-597. doi:10.3109/02656736.2013.807438

64. Sawhney N, Berjano EJ, Haemmerich D. Effect of electrode thermal conductivity in cardiac radiofrequency catheter ablation: a computational modeling study. *Int J Hyperthermia*. 2009;25(2):99-107. doi:10.1080/02656730802563051

65. Duck FA. *Physical Properties of Tissue: A Comprehensive Reference Book*. 1st ed. Academic Press; 1990.

66. Pennes HH. Analysis of tissue and arterial blood temperatures in the resting human forearm. *J Appl Physiol*. 1948;1(2):93-122. doi:10.1152/jappl.1948.1.2.93

67. Labonte S. Numerical model for radio-frequency ablation of the endocardium and its experimental validation. *IEEE Trans Biomed Eng*. 1994;41(2):108-115. doi:10.1109/10.284921

68. Obradovic M, Avilla A, Thiagalingam A, Filipovic N. Finite element modeling of the endocardial radiofrequency ablation. *J Serb Soc Comput Mech*. 2010;4(2):43-53.

69. Haines DE, Watson DD. A tissue heating during radiofrequency catheter ablation: a thermodynamic model and observations in isolated perfused and superfused canine right ventricular free wall. *Pacing Clin Electrophysiol*. 1989;12(6):962-976. doi:10.1111/j.1540-8159.1989.tb05034.x

70. González-Suárez A, Trujillo M, Koruth J, d'Avila A, Berjano E. Radiofrequency cardiac ablation with catheters placed on opposing sides of the ventricular wall: computer modelling comparing bipolar and unipolar modes. *Int J Hyperthermia*. 2014;30(6):372-384. doi:10.3109/02656736.2014.949878

71. Abraham JP, Sparrow EM. A thermal-ablation bioheat model including liquid-to-vapor phase change, pressure- and necrosis-dependent perfusion, and moisturedependent properties. *Card Electrophysiol Clin*. 2007;50(13–14):2537-2544. doi:10.1016/j.ijheatmasstransfer.2006.11.045

72. Zhao G, Zhang HF, Guo XJ, Luo DW, Gao DY. Effect of blood flow and metabolism on multidimensional heat transfer during cryosurgery. *Med Eng Phys*. 2007;29(2):205-215. doi:10.1016/j.medengphy.2006.03.005

73. Loiola BR, Orlande HR, Dulikravich GS. Approximate Bayesian computation applied to the identification of thermal damage of biological tissues due to laser irradiation. *Int J Therm Sci*. 2020;151:106243. doi:10.1016/j.ijthermalsci.2019.106243

74. Trujillo M, Bon J, Berjano E. Computational modelling of internally cooled wet (ICW) electrodes for radiofrequency ablation: impact of rehydration, thermal convection and electrical conductivity. *Int J Hyperthermia*. 2017;33(6):624-634. doi:10.1080/02656736.2017.1303751

75. Valvano JW, Cochran JR, Diller KR. Thermal conductivity and diffusivity of biomaterials measured with self-heated thermistors. *Int J Thermophys*. 1985;6(3):301-311. doi:10.1007/BF00522151

76. Shahidi AV, Savard P. A finite element model for radiofrequency ablation of the myocardium. *IEEE Trans Biomed Eng*. 1994;41(10):963-968. doi:10.1109/10.324528

77. Tungjitkusolmun S, Woo EJ, Cao H, Tsai JZ, Vorperian VR, Webster JG. Finite element analyses of uniform current density electrodes for radio-frequency cardiac ablation. *Am J Physiol-Heart Circ Physiol*. 2000;47(1):32-40. doi:10.1109/10.817617

78. Jacques SL, Gaeen M. Thermally induced changes in optical properties of heart. *IEEE Eng Med Biol Mag*. 1989;11(4):1199-1200.

79. Feng Y, Oden JT, Rylander MN. A two-state cell damage model under hyperthermic conditions: theory and in vitro experiments. *J Biomech Eng*. 2008;130(4):041016. doi:10.1115/1.2947320

80. Mackey MA, Roti Roti JL. A model of heat-induced clonogenic cell death. *J Physiol*. 1992;156(2):133-146. doi:10.1016/s0022-5193(05)80669-1

81. Walpot J, Juneau D, Massalha S, et al. Left ventricular mid-diastolic wall thickness: Normal values for coronary CT angiography. *Radiol: Cardiothoracic Imaging*. 2019;1(5):e190034. doi:10.1148/ryct.2019190034

82. Jain MK, Wolf PD. A three-dimensional finite element model of radiofrequency ablation with blood flow and its experimental validation. *IEEE Eng Med Biol Mag*. 2000;28(9):1075-1084. doi:10.1114/1.1310219

83. ASME V&V 20-2009. *Standard for Verification and Validation in Computational Fluid Dynamics and Heat Transfer*. ASME; 2009.